Generation and driving forces of plate-like motion and asymmetric subduction in dynamical models of an integrated mantle-lithosphere system

Tomoeki Nakakuki*

Chiho Hamada

Michio Tagawa

Department of Earth and Planetary Systems Science

Hiroshima University

1-3-1 Kagamiyama, Higashi-Hiroshima, 739-8526, JAPAN

accepted for publication in *Physics of Earth and Planetary Interiors*,

Dec. 4, 2007.

*Corresponding author

Tel: +81-82-424-6579

Fax: +81-82-424-6579

E-mail: nakakuki@hiroshima-u.ac.jp

Abstract

The dynamical effects of an asymmetric subduction structure on the generation of plate-like motion were investigated using two-dimensional numerical models of the integrated lithosphere-mantle system. To dynamically generate the plate boundary, we introduce a history-dependent rheology in which the yield strength is determined by past fractures. Only the buoyancy due to the internal density contrast consistently drives convective flow, including the motion of the viscous lithosphere, without imposed boundary conditions. We first investigate the effects of plate yield strength, friction at the plate boundary, and plate age on the emergence of plate-like motion with asymmetric subduction. Plate-like motion is generated when maximum plate strength is as high as that estimated by experimental rheology studies. The reason for this is that asymmetric subduction requires a plate-bending force much less than that for symmetric subduction because the plate gently bends when one-sided subduction occurs. In contrast, the strength of the plate boundary has to be very small for emergence of subduction, as several previous studies on the numerical convection and subduction modeling have pointed out. Development of the subducted slab is also controlled by the age of the plate. In the early stages of subduction, older plates increase their velocities faster because of their larger negative buoyancy. After the slab develops, the plate stiffness, that is, both the yield strength and the plate thickness, control plate velocity so that an older plate subducts more sluggishly. We next explore effects of viscosity layering in the underlying mantle, focusing on the mechanism in which the asthenosphere promotes plate motion. The low viscosity under the lithosphere enhances a mantle drag force that drives the plate, not only concentrating the convective flow beneath the plate but also enlarging its aspect ratio. We also examine longevity of the plate-like motion using the convection models with asymmetric subduction. The asymmetrically structured subduction process continues stably at high yield strength, at which episodic resurfacing or the

stagnant-lid mode occurs in the previous convection simulation studies. The asymmetric subduction structure therefore has key roles in generating plate-like motion as well as reducing the strength at the plate boundary.

Keywords
plate-like motion, mantle convection, asymmetric subduction, yield strength

1. Introduction

Understanding mechanisms that generate plate tectonics on the Earth is a fundamental issue of geodynamics. The construction of a dynamic mantle-convection model that includes plate tectonics is essential for directly solving this problem. Difficulty in developing numerical models arises from the complex rheology that causes lithosphere deformation in narrow regions such as faults. In the last decade, progress in both computer hardware and software has enabled us to incorporate more complex rheologies into high-resolution numerical models (reviewed by Tackley, 2000a; Bercovici, 2003).

The rheology with yielding as the continuum limit of fracture was introduced by Cserepes (1982) to produce plate-like behavior of the viscous lid. Weakening due to the yield stress induces focused deformation in the viscous lid and its plate-like movement. Plate-like motion is also produced in 3-D convection systems (Trompert and Hansen, 1998). The instantaneous yielding rheology, however, results in unstable behavior of the surface plate. Moresi and Solomatov (1998) and Tackley (2000b) systematically investigate the range of yield stress that generates stable plate motion using 2-D and 3-D models. They show that the yield strength should be much smaller than that estimated from experimental study (e.g., Kohlstedt et al., 1995) or from lithosphere deformation (Cloetingh and Wortel, 1986; Gerbault, 2000) to produce stable, plate-like motion. Tackley (2000c) and Richards et al. (2001) show that low asthenospheric viscosity improves plate motion stability, although the yield stress range is still far from experimental and observational study results. Tackley (2000c) introduces the damage rheology proposed by Bercovici (1996, 1998) into his 3-D models. He finds that the damage rheology does not improve the parameter range for generating plate-like motion. Ogawa (2003) surveys the broad range of damage rheology parameters using 2-D models. He concludes that the strength contrast between “intact” and “damaged” materials is important for generating satisfactorily rigid plate-like motion. Auth et al. (2003) have

performed high-resolution mantle convection simulations with the damage rheology to analyze the detailed damage rheology physics. They point out that advection of damage in the plate interior broadens deformation and depresses the stability of plate-like motion. Yoshida and Ogawa (2004) report the effects of uprising plumes on the emergence of new plate boundaries.

Convergent plate boundaries, reproduced by mantle convection models containing uniform rheology functions both with and without history dependence are still not realistic because the subduction structure produced is not one-sided, but two-sided. Davies (1989) imposes a dipped low-viscosity zone on the convection model with a temperature-dependent viscosity to simulate concentrated deformation at the plate boundary. In his model, plate-like motion is produced with asymmetric subduction of the viscous layer. Lenardic and Kaula (1994) show that the stagnant lithosphere becomes mobile when a low-viscosity layer is introduced at the top of the viscous lid, although they use convection models with a symmetric descending flow. Gurnis and his colleagues incorporate a weak fault acting as the plate boundary into mantle convection models (Zhong and Gurnis, 1995a, 1995b, 1996; Zhong et al., 1998; Gurnis et al., 2000). In their model, a one-sided subduction structure is also generated, and they point out that fault weakness is necessary to generate subduction. Honda et al. (2000) propose introducing a moving layer with yielding as an expression of history-dependent rheology to simulate a lubricating layer at the plate boundary, and they show the possibility of an asymmetric structure's emergence. The moving layer with yield stress is also employed in the models developed by Lenardic et al. (2000) and Moresi et al. (2002). These results imply that an advection effect of localized weakness caused by the heterogeneous rheology function is important to continuously generate asymmetric subduction with decoupled plate boundaries.

We believe that an Earth-like asymmetric subduction style has a key role in solving the discrepancy between the lithospheric strength of numerical models and rheology experiments. The reason why we expect this is that flexure of the

plate at trenches is not intense, but moderate in the case of one-sided subduction. Conrad and Hager (1999) and Schellart (2004) use kinematic numerical modelings and analog experiments to show that plate bending at a trench is an important resistance against plate motion. On the contrary, two-sided vertical subduction needs sudden buckling at the convergent zone to generate excessive lithospheric fracture. We therefore reexamine rheological parameter effects on determining lithospheric strength using dynamical models that reproduce one-sided subduction. For this purpose, we have developed numerical models of the lithosphere-mantle system in which asymmetric subduction occurs, introducing history-dependent yielding without imposed velocity boundary conditions. In our model, we observe the evolution of lithosphere deformation from initiation of subduction at the passive continental margin, with or without a preexisting weak zone, to the succeeding development of the subducted slab and plate motion.

First, we systematically investigate the effects of three variable parameters that determine plate strength—yield strength of the brittle-ductile transition layer in a lithosphere, the friction coefficient of the lithospheric brittle layer, and the friction coefficient of a fault zone at the plate boundary—on the emergence of subduction. We also consider effects of a preexisting weak zone on subduction generation for various plate strengths. Second, lithosphere age in the initial conditions is varied to examine lithosphere thickness effects. Third, forces acting on the plate are quantitatively analyzed to understand the dynamical mechanisms driving plate-like motion. The values of the driving forces obtained will be compared with a torque balance analysis (Forsyth and Uyeda, 1975). Fourth, the effects of viscosity layering are examined, especially focusing on the low-viscosity asthenosphere beneath the plate. Here, we vary temperature and pressure dependence of the viscosity to change the viscosity layering in the underlying mantle. We investigate the interaction of the plate with the underlying mantle, analyzing viscous coupling at the bottom of the lithosphere. Fifth, our models are integrated over a long time period to examine plate subduction

1 longevity and the plate motion evolution. We focus on the time-dependent
2 behavior of the subducted slab and on the plate motion driven by the slab's
3 negative buoyancy.
4
5
6

2. Model settings and basic equations

2.1 Model configuration

Figure 1 shows a schematic view of the model configuration. Here, we use a 2-D model with Cartesian geometry to minimize numerical difficulties, to handle a complicated rheology, and to perform high-resolution calculations. Physical parameters are described in Table I, and the model settings are found in Table II. In most cases, computations are performed to simulate the situation until the slab reaches 300 to 400 km, except in the long-term models. The time integration is less than 50 Myr, which is short enough to neglect internal heating. For the long time-integration model (Runs 100L and 102L, Table II), we also set the internal heating at zero because of the reason described in Section 3.5. In most cases, we set the height h of the model to be 1320 km (twice the upper mantle thickness), or 1500 km in the long time-integration. We use these values, which are less than or about half the mantle thickness, to maximize the model resolution. In the resolution-testing models, the height h is set at 660 km. The horizontal length l is changed depending on the age of the oceanic plate in the initial conditions (Table I), that is, a wider box is employed for models with older oceanic plates.

We consider subduction of the oceanic lithosphere beginning at a passive continental margin with or without a preexisting weak zone (Fig. 1). The models presented here therefore consist of two regions — "oceanic" and "continental." The "oceanic" region has an oceanic lithosphere and underlying mantle. The oceanic lithosphere is a surface layer with the same composition as that of the underlying mantle and a high viscosity due to its low temperature. The "continental" region consists of a continental lithosphere and underlying mantle. The continental lithosphere includes an intrinsically buoyant layer simulating a continental crust 35 km thick and a low-temperature mantle lithosphere beneath the crust. Because we consider a simulated margin at an immobile continent, the continental lithosphere is fixed at the right-side boundary (This effect will be

discussed briefly in section 4). The underlying mantle is identical to that of the oceanic region. In two cases (Runs 50-12 and 13, Table II), the buoyant crust is excluded. Namely, an overriding oceanic plate is also considered.

In our models, no external forces are imposed so that the driving forces of the system are generated internally by density anomalies. Subduction, however, is difficult to get started, and so we made the following assumptions. (1) A plume that provides a positive mantle drag force exists. (2) The initial temperature that produces a ridge-push force is set in the oceanic lithosphere. (3) The basalt-eclogite transition is neglected. (3) The power-law dislocation creep is parameterized as a low-viscosity channel. (4) The buoyancy of the basaltic layer in the subducting lithosphere is neglected. (5) A weak zone is introduced into most of the calculated models to produce a plate boundary in the initial conditions. These will be discussed in Section 4.

The temperature of the oceanic lithosphere in the initial conditions (Fig. 1a) is determined according to the half-space cooling model with 20, 50 and 100 Ma. The temperature of the continental lithosphere in the initial conditions is set to be horizontally uniform and the same as that of the oldest oceanic lithosphere. In the underlying mantle, the initial temperature T_i is set to be adiabatic and laterally homogeneous, namely,

$$T_i(z) = (T_M + T_0)\exp\left(\frac{\alpha g z}{C_p}\right) - T_0, \qquad (1)$$

where T_M is the mantle potential temperature (Celsius degree), T_0 is the absolute temperature of 0 °C, α is a thermal expansion coefficient, g is gravitational acceleration, and C_p is specific heat. We impose a hot thermal anomaly with dimensions of 50×400 km at the bottom-left corner to generate an upwelling plume that creates a mantle drag force on the bottom of the plate (Fig. 1) for the entire time. In this region, the potential temperature is set to be 200 K higher than

that of the surrounding mantle. This is a typical value of hot plume thermal anomalies (McKenzie and Bickle, 1988). In the long time-integration, the lower third of the model (1000 to 1500 km depth) has a fixed temperature provided by Eq. (1) because of a reason discussed in Section 3.5. In this case, the plume source with dimensions of 50×500 km is settled in the heat bath layer.

Mechanical boundary conditions for all the boundaries are set to be tangential-stress-free to satisfy the condition of having no external forces except buoyancy. The top boundary is set at a constant temperature T_0, and the bottom boundary is set at zero heat flux. Impermeable and insulated conditions are applied to both side boundaries.

2.2 Rheology model

We use a viscous fluid model to approximate the mantle flow. The rheology is expressed as a viscosity depending on temperature, pressure (depth), stress and yielding history. The viscosity at zero stress (η_0) is given by an Arrhenius-type equation as

$$\eta_0 = \min\left[A \exp\left[\frac{E^* + pV^*}{R(T + T_0)} \right], \eta_L \right], \quad (2)$$

where A is a pre-exponential factor, E^* is activation energy, p is hydrostatic pressure, V^* is activation volume, R is a gas constant and T is temperature. The symbol "min[a,b]" indicates a function to choose the smaller value of a and b. Here, we introduce the viscosity limit η_L to keep the numerical calculation accuracy. The estimated effective viscosity of the plate is on the order of 10^{24} to 10^{27} Pa from the lithosphere deformation study by Gordon (2000). We will briefly discuss the effects of this viscosity truncation on subduction generation in section 4. The values of E^* and V^* are based on those for olivine obtained by Karato and Wu (1993). We use three combinations of E^* and V^* for the short

time-integration models and one combination for the long time-integration models, as shown in Table II. Figure 2 shows the viscosity distribution with depth at initial temperature conditions for short time-integration models. A is fixed so that η_0 is equal to the reference viscosity $\eta_{ref} = 5 \times 10^{20}$ Pa (an average of the observed viscosity values in the upper mantle, Milne et al., 1999; Okuno and Nakada, 2001) at a depth of 410 km. The type I viscosity model (VM-I) has constant values of E^* and V^* obtained for the diffusion creep of wet olivine. The type II viscosity model (VM-II) has the same E^* as that of the Type I rheology, and V^* decreases with depth and is smaller than that of Type I by 50 % at the bottom of the model so that the viscosity becomes nearly constant beneath the lithosphere. The type III viscosity model (VM-III) has two viscosity layers divided at the depth of 410 km as shown in Fig. 2. In the upper layer, the values of E^* and V^* are determined based on the dislocation creep of wet olivine. The effect of the cubic power-law stress dependence is parameterized by reducing E^* and V^* to half their values (Christensen, 1984). This introduces a weak asthenosphere beneath the lithosphere because the larger value of V^* introduces a stronger pressure dependence than in VM-I. In the lower layer, the values of E^* and V^* are set to be the same as those of VM-I. The pre-exponential factors for the upper and lower layers are adjusted so that the viscosity values of both the layers become identical to each other at the boundary (410 km depth). In the case of the long time-integration model, we use a Type IIIa rheology (VM-IIIa) in which V^* decreases slightly with depth in the lower layer.

We introduce yield stress into the model to generate plate-like behavior in the surface viscous layer. The effective viscosity η is determined by von Mises' criterion as

$$\eta = \sigma_Y / 2\dot{\varepsilon}_{II} \quad \text{at} \quad \sigma_{II} = \sigma_Y \tag{3}$$

$$\eta = \eta_0 \quad \text{at} \quad \sigma_{II} < \sigma_Y , \tag{4}$$

where σ_Y is the yield stress as a function of the location, σ_{II} and $\dot{\varepsilon}_{II}$ are

second invariants of strain rate and viscous stress tensors defined by

$$\dot{\varepsilon}_{II} = \sqrt{\frac{1}{2}\sum_{i,j=1}^{2} \dot{\varepsilon}_{ij}^{\,2}} \tag{5}$$

and

$$\sigma_{II} = \sqrt{\frac{1}{2}\sum_{i,j=1}^{2} \sigma_{ij}^{\,2}} \quad . \tag{6}$$

Here, $\dot{\varepsilon}_{ij}$ is the strain rate tensor defined by

$$\dot{\varepsilon}_{ij} = \frac{1}{2}\left(\frac{\partial u_i}{\partial x_j} + \frac{\partial u_j}{\partial x_i} \right), \tag{7}$$

and the deviatoric stress tensor σ_{ij} is linked to $\dot{\varepsilon}_{ij}$ with constitutive relations as

$$\sigma_{ij} = 2\eta\dot{\varepsilon}_{ij} . \tag{8}$$

In most of the mantle except in a fault zone mentioned in the next paragraph, σ_Y simply depends on depth as

$$\sigma_Y = \min\left[Y_0 + c_Y \rho_0 g z, Y_{max} \right] \tag{9}$$

where Y_0 is a cohesive strength, c_Y is a friction coefficient of the brittle layer (Byerlee, 1978; Scholz, 1990) and Y_{max} is the maximum yield stress associated with the brittle-ductile transition (BDT) of the lithosphere (Kohlstedt et al., 1995).

Thus, the model lithosphere consists of three layers as shown in Fig. 3. We assume that Y_{max} is constant at depth, and treat it as a varying parameter in the surface layers (Fig. 3). The value of Y_{max} changes from 200 MPa, which is the stress level estimated from lithosphere deformation (Cloetingh and Wortel, 1986; Gerbault, 2000), to 600 MPa, which is about 1.5 times higher than that estimated from the experimental study (Kohlstedt et al., 1995). We also treat c_Y as a parameter that is assumed to vary from 0.2 to 0.3. This value of c_Y is smaller than the estimated value of 0.6 from an experimental rock fracture study (Byerlee, 1976) because weakening effects, such as hydration of the lithosphere, are considered. We do not include yielding in the continental surface layer to simulate stiff craton (Jordan, 1981), except in models without the continental crust (the overriding plate is "oceanic" and has no buoyancy) or the long time-integration models.

To introduce a "fault zone" for simulating the plate boundary, we introduce a moving segment whose yield stress is determined by its past yielding history. This simulates the segment whose mechanical strength is controlled by pore pressure due to water content and fault gouges. Here, we call this a "fault-zone segment." The yield stress hysteresis in the fault zone segment is shown in Fig. 4. The hysteresis of the yield stress is determined according to the following rule: The yield stress in fresh material in the fault zone segment is assumed to be the same as that of the normal lithosphere. Once yielding occurs in the fault zone segment, the yield stress σ_Y is reduced to a smaller value σ_F (Fig. 4), which is defined by

$$\sigma_F = c_F \rho_0 g z , \qquad (10)$$

where c_F is a friction coefficient of the "fractured" material. In order to indicate the positions of the fault segment and the fractured material, we introduce a "fault segment function" $\Gamma_F(x, z)$ and a "fractured segment function" $\Gamma_R(x, z)$. To settle the location of the fault-zone segment at the surface of the plate, we formally

introduce the function Γ_F. If the material becomes colder than a threshold temperature, T_h, we set a variable Γ_F at 1. The value of T_h is treated as a parameter (Table 2) to test its effects. Γ_F is advected independently of temperature by flow according to a mass transport equation,

$$\frac{\partial \Gamma_F}{\partial t} + \mathrm{u} \cdot \nabla \Gamma_F = 0 \qquad (11)$$

When the stress reaches σ_Y in the segment with $\Gamma_F = 1$ (the fault-zone segment), Γ_R is set to be 1 (the fractured fault segment). The yield stress in the segment with $\Gamma_R = 1$ is set to be σ_F. Γ_R is also transported by the flow according to Eq. (9). We assume that recovery of the damage occurs at a depth of 330 km, and then Γ_F and Γ_R are reset to zero. This depth must be deeper than about 150 km, which is the depth of the deformed overriding plate edge. We also set a weak zone at the top-left corner to simulate weakening by melting at mid-oceanic ridges. The yield strength there is set to be σ_F.

2.3 Basic equations

We use an extended Boussinesq fluid to include the adiabatic temperature influence on the viscosity layering in the model. The models presented here are governed by an equation of motion that includes an equation of continuity and a constitutive relation, an equation of state, an equation of energy, and an equation of mass transport. We use dimensional forms of the equations here because physical parameters are given by dimensional values due to the model's complexity. The equation of motion is expressed as

$$\left(\frac{\partial^2}{\partial x^2} - \frac{\partial^2}{\partial z^2} \right) \left[\eta \left(\frac{\partial^2 \Psi}{\partial x^2} - \frac{\partial^2 \Psi}{\partial z^2} \right) \right] + 4 \frac{\partial^2}{\partial x \partial z} \left(\eta \frac{\partial^2 \Psi}{\partial x \partial z} \right) = \frac{\partial \rho}{\partial x}, \qquad (12)$$

where Ψ is a stream function defined by

$$\boldsymbol{u} = (u, w) = \left(\frac{\partial \Psi}{\partial z}, -\frac{\partial \Psi}{\partial x} \right) \tag{13}$$

where (u, w) are x- and z-components of a velocity vector $\boldsymbol{u}$. The vertical axis is positive downward. An equation of state provides the density as

$$\rho = \rho_0 (1 - \alpha T) - \Delta\rho_c C \tag{14}$$

where ρ_0 is the mantle density at T = 0 °C, ρ_c is the density difference between the mantle and the continental crust, and C is a composition function to express the position of the continental crust (C = 1). C is governed by an equation of mass transport:

$$\frac{\partial C}{\partial t} + \mathrm{u} \cdot \nabla C = 0 . \tag{15}$$

The temperature is controlled by an energy equation including adiabatic heating and viscous dissipation:

$$\rho C_p \left[\frac{\partial T}{\partial t} + \mathrm{u} \cdot \nabla T + \mathrm{u} \cdot (\nabla T)_s \right] = k \nabla^2 T + \sum_{i,j=1}^{2} \sigma_{ij} \frac{\partial u_i}{\partial x_j} \tag{16}$$

with

$$\mathrm{u} \cdot (\nabla T)_s = w \frac{\alpha g (T + T_0)}{C_p}, \tag{17}$$

where k is thermal conductivity.

We employ a finite difference method based on a control volume scheme

to solve the equations (Nakakuki et al., 1994). We adopt uniform square control volumes of 5 km on each side for all the computations, except in one resolution test case. The number of control volumes is changed according to the size of the model, while the mesh size is fixed. The resolution test shows that the difference between the plate velocities in the 5-km resolution model and the 2.5-km resolution model is -2.8% after 2000 time steps and +2.5% after 4000 time steps. The overall features of both the models are very similar. We therefore believe that the 5-km grid has a sufficient resolution for the calculations presented in this paper. A modified Cholesky decomposition method is applied to solve the equation of motion (Eq. (12)). This makes the numerical solution stabilized against sharp viscosity variations greater than 10^6. To avoid numerical diffusion and phase errors of the mass transport equation (Eqs. (11) and (15)), a Cubic Interpolated Pseudo-particle method (CIP method) is adopted (Takewaki et al., 1985). The CIP method is a highly valid method for solving problems with sharp interfaces in computational fluid dynamics. Iwase and Honda (1992) confirmed its validity for mantle convection calculations. A first-order Euler method is applied to integrate the equation of energy (Eq. (16)) through time. The size of time steps is changed so that the maximum value of the Courant number $c_{i,j}$

$$c_{i,j} = \frac{u_{i,j}\delta t}{\delta x} + \frac{w_{i,j}\delta t}{\delta z} \qquad (14)$$

becomes equal to 0.1, where $u_{i,j}$ and $w_{i,j}$ are velocity components on the mesh, δt is a time-step interval, and δx and δz are mesh sizes for the x and z directions, respectively (but $\delta x = \delta z$ because we use a uniform square grid).

3. Results

We systematically investigated the effects of plate yield strength, friction at the plate boundary, plate age and viscosity layering in the underlying mantle on the generation of plate-like motion. Our models have many physical parameters because a complex rheology is required to reproduce the plate-like behavior of the surface layer. We have performed 50 runs in total, including 2 runs for the resolution test as shown in Table II. All simulations were started from conditions simulating a passive continental margin without a subducted slab (Fig. 1a). Details of model settings and variable parameters will be explained in the following sections.

3.1 Strength of the plate interior and the plate boundary

We first investigate influences of plate interior strength (c_Y, and Y_{max}), friction of the plate boundary, (c_F), and the style of the initial weak zone. We examine the Series 50 models here, in which VM-I's temperature- and pressure-dependent viscosity (Fig. 2) is used and the initial plate age is set to be 50 Ma. Three types of initial weak zone are considered as illustrated in Fig. 5. We place a segment with a history-dependent rheology at the ocean-continent plate boundary in all the cases. The initial strength of the fault segment is changed according to the initial conditions. Type-1 initial conditions (IC1, Fig. 5(a)) have a segment whose "fractured" yield strength is defined by Eq. (8). In IC1, the "fractured" segment penetrates to the bottom of the thermal boundary layer (depth of 150 km). In Type-2 initial conditions (IC2, Fig. 5(b)), the fractured fault segment reaches to the bottom of the continental crust (depth of 35 km). In Type-3 initial conditions (IC3), the segment does not have "fractured" strength so that the plate boundary has the same strength as that of ambient plate materials in the initial conditions.

Figure 6 shows the evolution of the viscosity field and the surface velocity for Run 50-01. This case has c_Y of 0.2, and Y_{max} of 200 MPa with IC1.

The oceanic (left) plate begins to subduct into the underlying mantle when the ascending plume starts to interact with the oceanic plate (26 Myr). The forces driving the plate will be discussed in Section 3.3. Asymmetric structure is first produced due to the asymmetric (i.e., dipped) configuration of the initial weak zone. The buoyancy of the continental crust is not always essential for initiating subduction (Run 50-12 and 13). Compression and bending of the subducting plate continuously generates damaged segments at the surface of the plate. This damaged region is advected into the shear zone by the lithosphere's motion. By this mechanism, the history-dependent rheology continuously produces the fault zone segment with weak strength at the plate boundary. The asymmetric structure is therefore maintained during slab growth. Figure 7 shows a snapshot of Run 50-01 in 46 Myr. The surface velocity (Fig. 7, top) and the stream lines show that the strain in the subducting lithosphere is concentrated at the plate boundary region and the internal segments of the high-viscosity layer very slightly deform so that the surface layer behaves as a rigid plate. Most of the lithosphere, except about 20 km near the ridge and 500 km near the trench, has a strain rate (s^{-1}) on the order of 10^{-18}. Both plate-like behavior of the lithospheric layer and one-sided subduction are produced.

We summarize the effects of initial conditions of c_Y and Y_{max} in the diagram shown in Fig. 8. In these cases, c_F is fixed at 0.01. In any case with IC1, oceanic plate subduction can be initiated even when Y_{max} 400 MPa with c_Y of 0.3. This value is comparable to the fracture strength estimated by Kohlstedt et al. (1995). The subduction structure is very similar when the viscosity-layering model is identical. When the partial weak zone (IC2) is assumed in the initial conditions, subduction of the plate is generated only in the case when Y_{max} = 100 MPa, and when Y_{max} = 200 and c_Y = 0.1 MPa. Introduction of stronger convective flow to the underlying mantle (Run 52-21) or the asthenosphere (Run 52-22) enables generation of subduction at Y_{max} of 200 MPa and c_Y of 0.2 (shown by the diamond in Fig. 8). Either increasing or decreasing the plate age does not affect subduction generation with IC2. The details are described in

Sections 3.2 and 3.4. In all the cases with IC3, subduction is not initiated.

We also examine the friction coefficient of the plate boundary (c_F). Here c_Y and Y_{max} are fixed at 0.2 and 200 MPa, respectively. Subduction is generated only when c_F = 0.01. Analysis of the driving/resisting forces of the plate shows that friction at the plate boundary accounts for a considerable amount of resistance against the plate motion (see Section 3.3). This value of c_F is much smaller value compared with Byerlee's law (Byerlee, 1978) for rock fracture (0.6). When c_F is larger than 0.01, the resistance from the overriding plate is too large for the driving force to generate subduction.

We test the threshold temperature of history-dependent rheology (T_h), that is, the effects of the fault segment thickness (run 50-08, 100-07 and 100L-03). The thickness systematically affects the plate velocity and the growth of the subducted slab. The style of the velocity variation is very similar, but the time elapsed to reach the same velocity is about 10 to 30 % longer. We can therefore only discuss relative effects of the rheological parameters on the evolution time and not absolute values.

3.2 Age of the oceanic plate and evolution of the plate motion

We next investigate effects of the oceanic plate age (A_P). The age of the plate in the initial conditions is set to be 20 Ma (Series 20), 50 Ma (Series 50), or 100 Ma (Series 100). The styles of the subducted slab are very similar in the three different models because the dip angle of the slab is strongly constrained by the initial weak zone. Figure 9 shows the evolution of the oceanic plate velocity for six models with A_P of 20, 50 and 100 Ma, Y_{max} of 200 and 600 MPa, and c_Y of 0.2 and 0.3.

In the case of 20 Ma (the red lines, Fig. 9), plate motion does not grow for 30 million years following inception but rapidly develops thereafter, because negative buoyancy does not grow large enough for the plate to founder into the mantle. The differences are very small in the early stages of evolution (t < 30 Myr). The evolution of plate motion is not affected by changing both c_Y and Y_{max}.

The reasons for this are that the brittle-ductile transition (BDT) layer does not exist (Fig. 3) because of the plate thickness, and that only the brittle layer of the plate causes a difference in plate strength. When the slab penetrates to a depth of more than about 200 km, the velocity dependence on Y_{max} appears, because Y_{max} has substantial strength effects on the subducted slab.

In the case of A_P = 50 Ma (the blue lines, Fig. 9), subduction grows faster than in the model with A_P = 20 Ma because the lithosphere has a more negative buoyancy. The internal plate strength (c_Y and Y_{max}) causes a larger difference in the evolution of plate velocity than in the case with A_P = 20 Ma. The friction coefficient c_Y is a more important parameter for determining the evolution of plate motion than Y_{max} because BDT layers (Fig. 3) occupy a significant portion of the surface plate only when c_Y = 0.3.

In the case of A_P = 100 Ma (the green lines, Fig. 9), the plate strength causes the largest difference of the plate motion evolution among the calculated models. In this case, Y_{max} differences affect the evolution of plate motion more than in the other cases. Before about 25 Myr, subduction develops faster in the cases with younger plates because older plates are heavier than younger plates, so older plates have larger driving forces. In the later stages, the plate with A_p = 100 Ma subducts more sluggishly than cases with younger plates because the thick plates have bending stiffness.

We also performed four calculations with IC2 (Run 20-21 at c_Y of 0.02 and Y_{max} of 200 MPa, Run 20-22 at c_Y of 0.02 and Y_{max} of 100 MPa, Run 100-21 at c_Y of 0.02 and Y_{max} of 200 MPa, and Run 100-22 at c_Y of 0.02 and Y_{max} of 100 MPa). The plate age does not affect the emergence of subduction because both the ridge-push force and fracture strength for generating the plate boundary increase proportionally with plate age.

3.3 Stress field and driving forces of the plate

We analyze stress fields and forces acting on the subducting plate to understand the driving force of subduction. Figure 10 shows the stress fields of

Run 50-01 in which plate-like behavior is produced. We define the "lithosphere" as a segment with temperature less than 1050 K or viscosity larger than 3×10^{21} Pa s, where the velocity is nearly constant. The boundary of the lithosphere is indicated with green lines in Fig. 10. We observe that high stress regions are settled in the lithosphere. This means that the plate propagates stress, or in other words, the plate acts as a stress guide. The normal stress is horizontal compression in most of the plate except in regions near a ridge or trench. The compressional stress is generally observed when plate-like behavior is generated in the surface. In this case, the tensional stress is produced in limited regions. Plate spreading near the ridge causes the tension. The plate bends downwards in the "outer rise" region near the trench so that tensional stress is induced in the upper side of the plate. The horizontal strain rate averaged in the outer rise region becomes negative, so that the plate is also compressed in this area. A wider region with tensional stress is generated in the case of VM-III (see section 3.5).

The evolution of forces acting on the plate for Run 50-02 with plate velocity and slab depth is shown in Fig. 11. We name the forces in Fig. 11b according to Forsyth and Uyeda (1975). We describe the forces acting on the plate by classifying them as driving forces (the solid lines, Fig. 11b) and resisting forces (the dashed lines, Fig. 11b). The driving force is generated by three sources, including pressure differences due to the shape of the plate (ridge-push force, RP), viscous drag due to convective flow in the underlying mantle (*driving* mantle-drag force, DF+), and negative buoyancy of the slab (slab-pull force, SP). RP is calculated from the pressure difference between the ridge and subdcution zone (Turcotte and Schubert, 1982), assuming that the compensation depth is 150 km. We neglect topographic uplift caused by the plume-ridge interaction because of the asthenosphere's low viscosity. The resisting force in the early stages of subduction consists of viscous stress from the underlying mantle (*resisting* mantle-drag force DF-), friction at the plate boundary (continental resistance, CR), and bending of the plate pushed by the overriding plate (plate bending, PB). Because viscous resistance against the

subducted slab (slab resistance, SR) is not significant for subduction initiation, it is not shown in Fig. 11b. The mantle-drag force (DF), which is the total viscous stress between the plate and the underlying mantle (Forsyth and Uyeda, 1975), acts as either an integrated driving or resisting force. DF is therefore separated into two parts, namely, DF+ and DF-, which are the integrals of shear stress dragging the plate in the moving and opposite directions. Plate bending (PB) is the same as a slab suction force (Forsyth and Uyeda, 1975).

In the initial stage of subduction, RP and DF+ account for the plate driving force. When a combination of RP and DF+ overcomes the resisting forces (CR and PB), the plate begins to move in the direction of the trench and to thrust under the overriding plate. RP increases with time because the plate becomes thicker with cooling. DF+ has 1/2 of RP's magnitude, but it has an important role in initiating subduction by dragging the plate in the early stages of subduction generation. Lack of DF+ force in a no-plume model (Run 50-11, Table II) initiates no subduction. When the upwelling plume interacts with the plate (near 30 Myr), DF+ increases and reaches an extremum (Fig. 11b). At the same time, the plate velocity sharply increases, and a small plate velocity peak is observed (Fig. 11a). CR and PB contribute a substantial portion of the force resisting plate motion. In the early stages, the magnitude of CR is slightly larger than that of PB. Although both CR and PB increase after 20 Myr, the increase of PB is more pronounced. The accelerating plate velocity induces an increase in plate yielding at the trench so that PB grows. The fault length is extended by plate thickening due to cooling with time and by deformation of the overriding plate entrained by the subducting plate. This causes CR to increase, as CR is proportional to the square of the fault length. The increase in CR and PB causes a momentary decrease in the plate velocity when the plate velocity is more than 2 cm yr^{-1}. Although c_F of 0.01 induces a significant resistive force in the magnitude of CR, subduction can be generated. Increasing c_F to 0.02 is enough to prevent the plate from subducting, because CR is proportional to c_F. SP increases as the subducted slab is developed, and finally dominates after the slab penetrates to a

depth of 120 km (Figs. 11a, b). After this time, the plate velocity grows quickly. DF- exceeds DF+ so that the mantle drag becomes resistive in total.

3.4 Viscosity layering and asthenosphere

We next consider effects of viscosity layering in the mantle, and we especially focus on the roles of the low-viscosity asthenosphere. We employ two types of viscosity structure (VM-II and VM-III, Fig. 2) other than the standard model (VM-I), changing the activation energy E^* and volume V^*.

Figure 12 shows snapshots of Run 52-01's viscosity field. In this case, the lower mantle has low viscosity so that the ascending flow of the hot plume is faster than that of the VM-I case in the lower mantle. We also assume a relatively weak lithosphere (c_Y = 0.1). A vigorous convection current driven by the upwelling plume induces a strong drag along the base of the lithosphere. In addition, the convection current is concentrated in the left half of the model because the underlying mantle has a nearly constant viscosity. The drag force pushes a part of the plate only near the ridge. These cause broad deformation of the lithosphere so that it does not behave like a rigid plate. If c_Y is assumed at 0.2, plate-like motion is generated (Run 52-02).

In the case of VM-III (Run 52-03 to Run 52-05), when the viscosity has a stronger pressure dependence in the upper layer of the mantle (Fig. 2), a distinctive low-viscosity layer is formed beneath the lithosphere (Fig. 12). The plate starts to move with greater velocity (4 cm yr^{-1}) than those of VM-I cases even before the upwelling plume directly contacts the bottom of the plate. The convective flow induced by the upwelling plume broadens horizontally because of the viscosity stratification (Fig. 12, bottom). This generates a drag force acting uniformly on the base of the lithosphere, so that the drag on the plate works more effectively in spite of the asthenosphere's low viscosity. In this stage, a tensional stress is observed around the 1000 km region near the trench. Moreover, the smaller E^* in VM-III causes a thinner mechanical plate than that in VM-I. This causes a smaller bending resistance of the subducting plate. The

plate velocity therefore grows faster than that of Run 50-01 does. The plate velocity of Run 52-03 reaches 12 cm yr^{-1} at its peak because the resistance from the ambient mantle is at a minimum. The velocity variation is larger than that of the VM-I rheology. The velocity of the plate is strongly changed by the viscosity layering structure.

Figure 13 shows the horizontal velocities for Run 50-01 (VM-I) and Run 52-03 (VM-III) at the centre of the model. The lines with solid symbols show the velocity when the driving mantle drag force is more dominant than the resisting force and the lines with open symbols show velocities in the opposite condition. In the former condition, the velocity beneath the plate becomes faster than that of the surface (plate) motion in Run 52-03. The asthenosphere promotes horizontal flow beneath the lithosphere. As Fig. 12 shows, the viscosity layering also causes the large aspect ratio of the underlying convective flow. The model's asthenosphere therefore enhances the driving force of the plate. Figure 14 shows the mantle-drag forces (both DF+ and DF-) of Run 50-01 (VM-I) and 52-03 (VM-III). The magnitude of DF+ in Run 52-03 is as large as that in Run 50-01 in spite of the 10-times-lower viscosity when DF+ becomes larger than DF-. The plate velocity increase (up to 12 cm yr^{-1}) in Run 52-03 induces the enlargement of DF- around 6 Myr. Because of the low viscosity in the asthenosphere, DF- in Run 52-03 is smaller than in Run 50-01 although the former's plate velocity is 3 times larger than that of the latter.

We also examine effects of viscosity layering on subduction generation when the initial weak zone is absent (Runs 52-21 and 52-22). The values of Y_{max} and c_Y are taken to be the same as those of Run 50-11, in which subduction cannot occur. In Run 52-11, strong dragging by the mantle flow causes subduction generation. In Run 52-12, subduction can be generated by the same mechanisms that encourage fast growth of the plate velocity in Run 52-03.

3.5 Longevity of the subduction and evolution of the slab

In the last analysis, we examine subduction longevity and evolution of

the subducted slab. For this purpose, we execute the model as long as CPU time permitted. Because each run takes about 500 hours of CPU time, we perform 4 runs with different asthenosphere settings (Runs 100L and 102L), "fault zone segment" thicknesses (Run 102L-02), and lithospheric internal strengths (Run 102L-03). Because we are focusing on the plate and the upper mantle slab dynamics, the temperature in the lower 500 km of the model is fixed to the mantle adiabatic temperature to avoid having the slab stagnant above the bottom of the model layer. The other important advantage is that the underlying mantle temperature is constant in time. We can therefore remove the effects of temperature-dependent viscosity variations to focus on stability and longevity of the subducting slab. We use the VM-Ia (Run 100L-01) and VM-IIIa (Runs 102L-01 to 03) viscosity layering (Section 2.2) in which V^* in the lower layer is slightly reduced with depth (Table I) so that the velocity of the plate becomes about 5 to 10 cm yr^{-1}. In addition, the rheology of the overriding plate may affect its stability. We therefore introduce yielding into the continental crust layer, and set the E^* and V^* (Table I) in this layer to match those of granite (Kohlstedt et al., 1995). This, however, does not affect longevity of the plate motion.

Figure 15 shows snapshots of the viscosity field for Run 102L-02. The subduction and plate-like motion of the surface layer continue to the end of the calculations. In the cases with a low-viscosity asthenosphere (Runs 102L), the deeply subducted slab swings because the high-viscosity deep mantle resists the descending slab. When the subducted slab is convex (65 Myr in Fig. 15), the plate moves slightly faster than when it is nearly vertical or concave (53 Myr). Small-scale instabilites beneath the lithosphere occur with fluctuations of the uprising flow (43 to 128 Myr). These quickly disappear after the uprising plume becomes stationary. Afterwards, new instabilities are generated beneath the lithosphere older than 60 Ma (148 Myr). The small-scale instabilities are not observed in the case with a more viscous asthenosphere (100L-01).

The velocities of the subducting plate for Run 100L-01 through 102L-03 are shown in Fig. 16. In the case of Run 100L-01 without the low-viscosity

layer, the velocity converges to 4 - 5 cm yr^{-1}. In Runs 102L-01 to 03 with the low-viscosity asthenosphere, the velocities peak at 8 - 9 cm yr^{-1} when the slab is sinking at a depth around 300 km. After that, the plate velocity finally converges to 4 - 5 cm yr^{-1} in Runs 102L-01 and 02 and 3.5 - 4.5 cm yr^{-1} in Run 102L-03. The low-viscosity asthenosphere, therefore, does not significantly influence the plate motion after the subducted slab develops. The plate motion under the larger yield stress condition (600 MPa, Run 102L-03) is slightly less than that under the smaller yield stress condition (300 MPa, Run 102L-01). The thickness of the "fault zone segment" does not affect the terminal plate motion velocity (Run 102L-02). Because resistance to the subducted slab is the largest of the resistive forces, the mantle viscosity predominantly controls the descending velocity of the developed slab. Fluctuation of the plate velocity after it reaches terminal velocity is caused by slab deformation in the depth-dependent viscosity layering. The slab is vertically compressed because the tip of the slab receives greater viscous resistance than the shallower part does.

4. Discussion

We construct integrated numerical models of the plate-mantle system to investigate effects of asymmetric subduction structures on the generation of surface plate-like motion under various plate strengths and tectonic settings. In our models, introducing a history-dependent yield strength is important for generating an asymmetric subduction structure. Our proposed history- dependent yield strength is similar to the limit of the damage rheology model (Auth et al., 2003), proposed first by Bercovici (1996), with extremely strong temperature dependence, fast damage growth, and slow damage healing. The sharp temperature dependence in the generation of fractures is able to produce asymmetry because the position of the weak zone is limited to the plate surface. In cases with gentler temperature dependence, symmetric subduction over a broader plate boundary area would be produced. The advection of past fractures preserves the damage and its asymmetric distribution, promoting consecutive weak zones at the surface of the subducting plate. On the contrary, the damage advection term is smaller than the source and healing terms in models with a damage rheology (Ogawa, 2003; Auth et al., 2003). This may induce symmetric subduction.

We first show that the emergence of plate-like motion with subduction is insensitive to the brittle-ductile transition (BDT) strength of the plate interior, but sensitive to friction on the plate boundary. If the plate boundary strength is small enough, subduction occurs even at the highest BDT strength value (600 MPa). Subduction generation does not strongly depend on the plate strength because Earth-like asymmetric subduction needs a small degree of weakening for the lithosphere to bend and allow the plate to drop into the mantle at the trench. Yielding in the whole plate must occur to generate symmetric subduction. In this case, the plate bending force (PB) has to be on the order of 10^{13} N m^{-1} with Y_{max} = 200 MPa. The PB for asymmetric subduction (Fig. 11b) is much smaller than that for symmetric subduction, although it is a significant resistive force. The

subducted slab can be formed when the friction coefficient (c_F) of the fault zone at the plate boundary is small (≤ 0.01). This value may be extraordinarily small, so that excessive reduction of the plate boundary strength due to hydration at the plate boundary (e.g., Jambon and Zimmermann, 1990) is therefore necessary to generate subduction. Sensitivity to the plate boundary strength was predicted by McKenzie (1977), and it is consistent with the conclusions of previous studies (Toth and Gurnis, 1998; Conrad and Hager, 1999) focused on initiation of asymmetric subduction. In our models, resistance at the plate boundary (CR) accounts for the largest portion of resistive force in the early stages of subduction. The friction coefficient c_F corresponds to CR, which is the integral of friction along the fault. When the plate thickness reaches the level attained at 100 Ma, the c_F value of 0.005 coincides with the mean CR/RP ratio obtained by torque-balance analysis (Forsyth and Uyeda, 1975). The friction coefficient expected from observational studies should be even smaller than that employed here. If that is true, the plate bending force (PB) is the largest of the resistive forces.

When the initial conditions do not include the weak zone (IC3, Fig. 6), a subducted plate cannot be generated under any conditions using the yield strength in our models. To generate fault zones in the intact lithosphere, the magnitude of the force must be on the order of 10^{13} N m^{-1}, which is the integral of the plate's internal strength. Among the forces considered here, only the slab pull (SP) can provide that level of force. Introduction of a partial initial weak zone (IC2, Fig. 6) can initiate subduction when the yield strength is as small as 200 MPa (Fig. 8). With a larger maximum plate strength, an initial weak zone as deep as the bottom of the lithosphere (IC1) is required to initiate subduction. Mechanisms at least partially responsible for fracturing the plate, such as sediment loading (Cloetingh et al., 1982; Branlund et al., 2001; Regenauer-Lieb et al., 2001), plume intrusion (Turcotte et al., 1977; Kemp and Stevenson, 1996), or transformation of past fracture zones (Gurnis et al., 2000), would be important for generating new subduction when we introduce neither a weak zone

nor smaller plate strength. If subduction is initiated by these mechanisms, a drag force (DF+) exerted by the underlying convective flow is also important to bend the plate until the slab-pull force is enlarged. Hall et al. (2003) have succeeded in spontaneously producing a developed subduction with backward slab motion under a thin overriding lithosphere using 2-D dynamic models.

In our model, the upwelling plume beneath the ridge is introduced to generate a positive mantle drag force (DF+). The combination of DF+ and RP is necessary to initiate subduction. This does not mean that the uprising plume must couple with the ridge. If the approximate direction of mantle flow is the same as sea floor spreading, the asthenosphere can be expected to act as DF+ pushes the lithosphere. In cases with a low-viscosity asthenosphere (Runs 52 and 102L), subduction is initiated without direct interaction between the uprising plume and the overlying plate.

In the early stages of subduction, the old plate slab (100 Ma) develops faster than the young plate (20 Ma) because the older plate has more negative buoyancy. In the case of young plates, the lack of negative buoyancy causes subduction to start after the upwelling plume pushes the plate directly. The plate motion slows in the later stages of the older-plate case when the slab thrusts under the bottom of the overriding plate. In this situation, resistance by PB and CR controls the plate motion, and PB is more dominant than CR. The difference in strength and thickness of the BDT layer significantly affects growth of the subducted slab. This is similar to the situation in which the plate bending force dominates and governs plate motion, as pointed out by Conrad and Hager (1999) and Schellart (2004). Later, with a more mature slab, the plate motion is constrained by slab resistance (SR) in our viscosity model. A mantle-drag force (DF) also provides resistance in this stage, as is consistent with observed plate-driving forces (Forsyth and Uyeda, 1975).

The physical mechanism in which the asthenosphere promotes plate motion is quantitatively revealed by analysis of mantle-drag forces (Fig. 14). The mantle-drag force provides an important portion of the driving force in the early

stages of subduction. The viscosity layering reinforces the effect of mantle drag, because this generates a horizontal large-scale flow concentrated in the low-viscosity layer. The asthenosphere therefore promotes generation of plate motion. Because the power-law rheology is parameterized as a low-viscosity layer, the effect of a non-Newtonian rheology on reducing viscosity might be overestimated during early evolution when plate motion is not active. In this case, the early evolution of subduction would be slower than that in our calculation. The low-viscosity layer can, however, be produced by convection in the underlying mantle. In this case, our parameterization using the low viscosity layer would be reasonable. When the slab is developed, the mantle drag acts as a resistive force, as in the case with weaker viscosity layering. In this situation, the underlying low-viscosity mantle does not impede the plate motion so strongly as a higher-viscosity mantle. These mechanisms would cause the stabilization of plate-like motion as pointed out by Tackley (2000c) and Richards et al. (2001). Peak plate velocity reaches a larger value here than in the case without the asthenosphere layer because of the smaller resistance against the plate and the subducted slab. This means that the viscosity of the asthenosphere is also important for controlling plate motion as well as plate strength before SR becomes dominant.

Our models with long time-integrations show that the subduction continues stably over a long period (> 100 Myr) at the high yield strength (≥ 200 MPa). In this level of the yield strength, previous simulations with uniform yielding rheologies show that episodic or stagnant-lid convection occurred (Moresi and Solomatov, 1998; Trompert and Hansen, 1998; Tackley, 2000b). The symmetric subduction process seems to be unstable. On the contrary, the asymmetric subduction is stable because of the gentle lithospheric bending. In the early stages of subduction, the velocity of plate motion depends on plate strength and the asthenosphere's viscosity. As the slab reaches the high-viscosity layer, the plate motion slows and converges to a very similar speed. This means that the viscosity of the surrounding mantle is the most

important factor controlling the sinking velocity of the mature slab in our models. If the deep mantle has lower viscosity, there is a possibility that the plate motion is controlled, on the contrary, by plate strength. A more systematic study may be needed to reveal quantitatively which mechanism dominates in determining plate motion. We neglect the effect of mantle thickness in the long time-integration models because of computer capacity. We assume the lowermost mantle has fixed temperature (Section 3.5) because we focus on the effects of one-sided subduction structures on time-dependent plate motion behavior, avoiding stagnation of the slab at the bottom of the model, which is thinner than the Earth's mantle. We anticipate that stagnation at the bottom does not affect this situation because the slab migrates (Engebretson et al., 1992) when the trench is not fixed. We still need to examine the interaction of the slab with the lowermost mantle in the future.

We neglect the negative buoyancy of the 410-km phase transition and the basalt-eclogite phase transition in the subducted basaltic crust (e.g. Irifune, 1993). The former increases the slab-pull force by $\sim 1 \times 10^{13}$ N m^{-1} (Turcotte and Schubert, 1982) and the latter increases it by $\sim 5 \times 10^{12}$ N m^{-1}. The speed of the plate motion when a slab penetrates the transition zone is expected to increase about 100%. The phase transition at the 660 km depth affects the fate of the subducted plate (Christensen and Yuen, 1984). Seismic tomography images show that the slab structure either stagnates in the transition zone or penetrates the lower mantle (e.g., reviewed by Fukao et al., 2001). Our models presented here are useful for investigating the interaction of the subducting plate with phase transitions. The phase boundaries also strongly change the time-dependent convection behavior (Machetel and Weber, 1991; Honda et al., 1993; Tackley et al., 1993) and influence the plate velocity (Christensen and Yuen, 1984; Schmeling et al., 1999). The interaction between the basaltic layer and the 660 km transition zone may also affect the plate motion (van Keken and Karato, 1996).

The viscosity jump at the 660 km phase transition controls the structure

of subduction (Gurnis and Hager, 1988; Enns et al., 2005) and influences plate motion. Modeling the present plate motion using 3-D instantaneous calculations (Yoshida et al., 2001) also indicates a weak coupling of the plate motion and the lower mantle. Reduction of slab strength due to the grain-size reduction associated with the phase transition is predicted by high-pressure mineralogy (Rubie, 1984; Riedel and Karato, 1997) and is consistent with observations of the geoid (Moresi and Gurnis, 1996). The effects of mantle transition zone slab strength on plate motion (Conrad et al., 2004) are subjects to be studied in the future.

We focus on the effects of plate yield strength so that the plate rheology is treated as a pure viscous fluid with yielding. Elasticity in a Maxwell fluid takes part of the plate deformation so that introduction of elasticity can be expected to promote, not to impede, plate motion. It is important to quantitate viscoelastic effects (e.g., Moresi et al., 2002). We also assume the viscosity truncation at η_L of 10^{25} Pa s. We have studied the influence of setting η_L in the range estimated from observed plate deformations (Gordon, 2000). The viscosity truncation at 10^{24}, 3×10^{24}, and 10^{26} Pa s changes the peak velocity of the plate by +12.4%, +7.5% and -2.5% (Tagawa et al., 2007). The viscosity truncation does not significantly affect plate motion because yielding controls plate motion.

We use a fault segment thicker than 15 to 25 km in the model because of computing resolution limitations. In this study, we have introduced a threshold temperature for a history dependent rheology (T_h) that controls thickness of damaged material. We believe that the wetness of an oceanic crust lubricates a the plate boundary although that it is much thinner than the fault segment in our models. We have therefore examined whether or not a history-dependent layer with the same thickness as the oceanic crust (6 km) is enough to work as the plate boundary (Tagawa et al., 2007). Our results show that a thin wet oceanic crust works well as the plate boundary when the strength is as low as that employed in this paper with the same internal lithospheric strength.

The other main simplification is that our models have one subduction

zone consisting of two plates in a 2-D rectangular box so that we can attain the highest resolution possible given the present computer capacity. Moreover, the overriding plate is fixed at the boundary of the model. We have examined the effects of a movable overriding plate (Tagawa et al., 2007) previously, and these results show that one-sided subduction is produced in a freely mobile overriding plate with or without crustal buoyancy. In this case, trench migration is observed. Two-dimensional models, however, can simulate very limited features of plate-boundary reorganization. Three-dimensional models are required for investigating the reorganization of the plate boundary. The computation of a high-resolution 3-D model with large viscosity variations is still very difficult and requires too much CPU time. The treatment of the plate boundary at the subduction zone proposed in this study would be practical in 3-D models.

5. Conclusions

We have shown that one-sided structure of subduction is key for generating plate-like motion using 2-D integrated plate-mantle models. We summarize the dynamical effects of asymmetric structure on the generation of plate-like motion as follows:

(1) The generation of plate-like motion with asymmetric subduction is reproduced with a wide range of strengths of the plate interior. This occurs because asymmetric subduction requires a plate-bending force much less than that required for symmetric subduction to yield gentle plate bending.

(2) Friction at the plate boundary must be strongly lower than the internal plate strength to generate plate-like motion contrary to (1), as previous studies on the numerical convection (Tackley, 2000c; Ogawa, 2003) and subduction (Toth and Gurnis, 1998; Conrad and Hager 1999) modeling have pointed out.

(3) The age of the plate affects evolution of plate motion in the early stages of subduction mainly because of its relationship with negative buoyancy. Plate strength effects are more distinguished because the thickness of the brittle-ductile transition layer, which controls plate bending, increases with plate age.

(4) The asthenosphere promotes plate-like motion because it enhances the effects of the mantle drag force. This occurs because viscosity stratification concentrates the convective flow and enlarges its horizontal scale beneath the plate. Viscosity layering strongly varies the plate velocity in the early stages of subduction because the asthenosphere provides viscous resistance to the subducted slab.

(5) The plate continues asymmetric subduction stably for a long time after the slab is mature even if the plate has a yield strength as high as that in situations with unstable symmetric downwelling.

Acknowledgements

The authors thank S. Honda for his stimulating discussions. They are grateful to H. Fujimoto for his comments. They also thank two anonymous reviewers for their thorough and constructive reviews. The computation time on NEC SX Computer and Hitachi SR11000 System was provided at the Institute for Non-linear Science and Mathematics (INSAM), and the Information Media Center (IMC), Hiroshima University. Most of the figures are plotted using the Generic Mapping Tools (GMT) developed by Wessel and Smith. This study is partly supported by the Grant-in-Aid for Scientific Research (No. 16340130) from the Japan Society for the Promotion of Science.

References

Auth, C., Bercovici, D., Christensen, U. R., 2003. Two-dimensional convection with a self-lubricating simple-damage rheology. Geophys. J. Int. 154, 783-800.

Bercovici, D., 1996. Plate generation in a simple model of lithosphere–mantle with self-lubrication. Earth Planet. Sci. Lett. 144, 41-51.

Bercovici, D., 1998. Generation of plate tectonics from lithosphere–mantle flow and void-volatile self-lubrication. Earth Planet. Sci. Lett. 154, 139-151.

Bercovici, D., 2003. The generation of plate tectonics from mantle convection. Earth planet. Sci. Lett. 154, 139-151.

Billen, M., Gurnis, M, 2001. A low viscosity wedge in subduction zones. Earth Planet. Sci. Lett. 193, 227-236.

Branlund, J. M., Regenauer-Lieb, K., Yuen, D. A., 2001. Weak zone formation for initiating subduction from thermo-chemical feedback of low-temperature plasticity. Earth Planet. Sci. Lett. 190,237-250.

Byerlee, J., 1978. Friction of rocks. Pure Appl. Geophys. 116, 615-626.

Cloetingh, S., Wortel, R., Vlaar, N. J., 1982. Evolution of passive continental margins and initiation of subduction zones. Nature 297, 139-142.

Cloetingh, S., Wortel, R., 1986. Stress in the Indo-Australian plate. Tectonophys. 132, 49-67.

Christensen, U. R., 1984. Convection with pressure- and temperature-dependent non-Newtonian rheology. Geophys. J. R Astron. Soc. 77, 343-384.

Christensen, U. R., Yuen, D. A., 1984. The interaction of a subducting lithospheric slab with a chemical or phase boundary. J. Geophys. Res. 89, 4389-4402.

Conrad, C. P., Hager, B. H., 1999. Effects of plate bending and fault strength at subduction zone on plate dynamics. J. Geophys. Res. 104, 17551-17571.

Conrad, C. P., Lithgow-Bertelloni, C., 2004. The temporal evolution of plate

driving forces: Importance of “slab suction” versus “slab pull” during Cenozoic. J. Geophys. Res. 109, doi10.029/2004JB002991.

Cserepes, L., 1982. Numerical studies of non-Newtonian mantle convection. Phys. Earth Planet. Int. 30, 49-61.

Davies, G. F., 1989. Mantle convection model with a dynamic plate: topography, heat flow, and gravity anomalies. Geophys. J. 98, 461-464.

Engebretson, D. C., Kelley, K. P., Cashman H. J., Richards, M. A., 1992. 180 million years of subduction. GSA today 2, 93-100.

Enns, A., Becker, T. W., Schmeling, H., 2005. The dynamics of subduction and trench migration for viscosity stratification, Geophys. J. Int., 160, 761-775

Forsyth, D., Uyeda, S., 1975. On the relative importance of the driving forces of plate motion. Geophys. J. R. Astron. Soc. 142, 163-200.

Fukao, Y. Widiantro, S, Obayashi, M., 2001. Stagnant slabs in the upper and lower mantle transition region. Rev. Geophys. 39, 291-323.

Gerbault, M. 2000. At what level is the central Indian Ocean lithosphere buckling. Earth Planet. Sci. Lett. 178, 165-181.

Gordon, R. G., 2000, Diffuse oceanic plate boundaries: Strain rate, vertically averaged rheology and constraints with narrow plate boundaries and stable plate interiors, in The history and Dynamics of Grobal Plate Tectonics. Geophys. Monograph Series Vol. 121, pp143-159, ed. Richards, M. A. Gordon, R. G., van der Hirst, R., Am. Geophys. Union, Washington, DC.

Gurnis, M. , Zhong, S., Toth, J., 2000. On the competing roles of fault reactivation and brittle failure in generating plate tectonics from mantle convection, in The history and Dynamics of Grobal Plate Tectonics. Geophys. Monograph Series Vol. 121, pp73-94, ed. Richards, M. A. Gordon, R. G., van der Hirst, R., Am. Geophys. Union, Washington, DC.

Hall, C. E., Gurnis, M., Sdrolias, M., Lavier, L. L., and Müller, R. D., 2003. Catastrophic initiation of subduction following forced convergence across fracture zones, Earth Planet. Sci. Lett. 212, 1530.

Honda, S., Yuen, D. A., Balachander, S. Reuteler. D., 1993. Three-dimensional instabilities of mantle convection with multiple phase transitions. Science 259, 1308-1311.

Honda, S., Nakakuki, T., Tatsumi, Y., and Eguchi, T., 2000. A simple model of mantle convection including past history of yielding. Geophys. Res. Lett. 27, 1559-1562.

Iwase, Y. & Honda, S., 1993. Deformation of the crust and upper mantle beneath the back-arc caused by subduction. J. Phys. Earth 41, 347-363.

Jambon, A., Zimmermann, J. L., 1990, Water in oceanic basalts: Evidence for dehydration of recycled crust, Earth Planet. Sci. Lett., 90, 297-314.

Jordan, T. H., 1981. Continents as a chemical boundary layer. Philos. Trans. R. Soc. London Ser. A 301, 359-373, 1981.

Karato, S., Wu, P., 1993. Rheology of the upper mantle: a synthesis. Science 260, 771-778.

Kohlstedt, D. L. Evans, B., Mackwell, S. J., 1995. Strength of the lithosphere: Constraints provided by the experimental deformation of the rocks. J. Geophys. Res., 100, 17587-17602.

Kemp, D. V., Stevenson, D. J., 1996. A tensile flexural model for the initiation of subduction. Geophys. J. Int. 125, 73-94.

Lenardic, A., Kaula, W. M., 1994. Self-lubricated mantle convection: Two-dimensional models. Geophys. Res. Lett. 21, 1707-1710.

Lenardic, A., Moresi, L., Mühlhaus, H., 2000. The role of mobile belts for the longevity of deep cratonic lithosphere: The crumple zone model. Geophys. Res. Lett. 27, 1235-1238.

Machetel, P. and Weber, P., 1991. Intermittent layered convection in a model mantle with an endothermic phase change at 670 km. Nature 350, 55-57.

McKenzie, D. P., 1977. The initiation of trenches: A finite amplitude instability, in Island arc, deep sea trenches and back-arc basins. Maurice Ewing Series Vol. 1, pp. 57-61, ed. Talwani, M., Pitman, W. C., Am. Geophys. Union, Washington, D. C.

McKenzie, D. Bickle, M. J., 1988. The volumes and composition of melt generated by extenstion of the lithosphere, J. Petrol. 29, 625-679.

Milne, G. A, Mitrovica J. X., Davis J. L., 1999. Near-field hydro-isostacy: the implementation of a revised sea-level equations. Geophys. J. Int. 139, 464-482.

Moresi, L., Gurnis, M., 1996. Constrains on the lateral strength of slab from three-dimensional dynamic flow models. Earth Planet. Sci. Lett. 138, 15-28.

Moresi, L. & Solomatov, 1998. V. Mantle convection with brittle lithosphere: thoughts on the global styles of the Earth and Venus. Geophys. J. Int. 133, 669-682.

Moresi, L., Dufour, F., Mühlhaus, H.-B., 2002. Mantle convection with viscoelastic/brittle lithosphere: numerical methodology and plate tectonic modeling. Pure Appl. Geophys. 159, 2335-2356.

Nakakuki, T., Sato, H., Fujimoto, H., 1994. Interaction of the upwelling plume with the phase and chemical boundary at 670 km discontinuity: Effects of temperature-dependent viscosity. Earth Planet Sci. Lett. 121, 369-384.

Okuno, J. Nakada, M. 2001. Effects of water load on geophysical signals due to glatial rebound and implication for mantle viscosity. Earth Planet Space 53, 1121-1135.

Ogawa, M., 2003. Plate-like regime of a numerically modeled thermal convection in a fluid with temperature-, pressure- and stress-history-dependent viscosity. J. Geophys. Res. 108, doi: 101029/2001JB000069.

Peacock, S. M., 1996. Thermal and petrologic structure of subduction zones, in Subduction Top to Bottom. Geophys. Monograph Series, vol. 96, pp. 119-133, ed. Bebout, G. E., Scholl, D. W., Kirby, S. H., Platt, J. P., Am. Geophys. Union, Washington, D. C.

Regenauer-Lieb, K., Yuen, D. A., Branlund, J., 2001. The initiation of subduction: Criticality by addition of water?, Science, 294, 578-580.

Richards, M., Yang, W.-S., Baumgardner, J. R., Bunge, H.-P., 2001. Role of a

low-viscosity zone in stabilizing plate tectonics: Implication for comparative terrestrial planetology. Geochem. Geophys. Geosyst. 2, 2000GC000115.

Riedel, M. R., Karato, S., 1997. Grain-size evolution in subducted oceanic lithosphere associated with the olivine-spinel transformation and its effects on rheology. Earth Planet. Sci. Lett. 148, 27-43.

Rubie, D. C., 1984. The olivine-spinel transformation and the rheology of subducting lithosphere. Nature 308, 505-508.

Schellart, W. P., 2004. Quantifying the net slab pull force as a driving mechanism for plate tectonics. Geophys. Res. Lett. 31, doi: 101029/2004GL019528.

Schmeling, H., Monz, R., Rubie, D. C., 1999. The influence of olivine metastability on the dynamics of subduction. Earth Planet. Sci. Lett. 165, 55-66.

Scholz, C. H., 1990. The mechanics of earthquakes and faulting. 439pp., Cambridge University Press, Cambridge.

Tackley, P. J., 2000a. Mantle convection and plate tectonics: Towards an integrated physical and chemical theory. Science 288, 2002-2007.

Tackley, P. J., 2000b. Self-consistent generation of tectonic plate in time-dependent, three-dimensional mantle convection simulations 1. Pseudoplastic yielding. Geochem. Geophys. Geosyst., 1, 2000GC000,036.

Tackley, P. J., 2000c. Self-consistent generation of tectonic plate in time-dependent, three-dimensional mantle convection simulations 2. Strain weakening and asthenosphere. Geochem. Geophys. Geosyst. 1, 2000GC000,043.

Tackley, P. J., Stevenson, D. J., Glatzmaier, G. A., Schubert, 1993. Effects of an endothermic phase transition at 670 km depth on spherical mantle convection. Nature 361, 699-704.

Tagawa, M., T. Nakakuki, M. Kameyama, F. Tajima, 2007. The role of history-dependent rheology in plate boundary lubricator for generating one-

sided subduction, Pure Appl. Geophys., 164, 879-907.
Takewaki, H., Nishiguchi, A., Yabe, T., 1985. Cubic interpolated pseudo-particle method (CIP) for solving hyperbolic-type equations. J. Comp. Phys. 61, 261-268.
Toth, J., Gurnis M., 1998. Dynamics of subduction initiation at preexisting fault zones. J. Geophys. Res. 103, 18053-18607.
Trompert, R. Hansen, U., 1998. Mantle convection simulations with rheologies that generate plate-like behavior. Nature 395, 686-689.
Turcotte, D. L., Haxby, W. E., Ockendon, J. R., 1977. Lithospheric instabilities, in Island arc, deep sea trenches and back-arc basins. Maurice Ewing Series Vol. 1, pp. 63-69, ed. Talwani, M., Pitman, W. C., Am. Geophys. Union, Washington, D. C.
Turcotte, D. L., Schubert, G., 1982. Geodynamics. 450pp., John Wiley & Sons, Inc., New York.
Yoshida, M., Honda, S., Kido, M. Iwase, Y., 2001. Numerical simulation for the prediction of the plate motions: Effects of lateral viscosity variations in the lithosphere. Earth Planet Space 53, 709-721.
Yoshida, M. Ogawa, M., 2004. The role of hot uprising plume in the initiation of plate-like regime of three-dimensional mantle convection. Geophys. Res. Lett. 31, L05607, doi:10.1029/2003GL017376.
Zhong, S., Gurnis, M., 1995a. Mantle convection with plates and mobile, faulted plate margins. Science 267, 838-843.
Zhong, S., Gurnis, M., 1995b. Towards a realistic simulation of plate margins in mantle convection. Geophys. Res. Lett. 22, 981-984.
Zhong, S., Gurnis, M., 1996. Interaction of weak faults and non-Newtonian rheology produces plate tectonics in a 3D model of mantle flow. Nature 383, 245-247.
Zhong, S., Gurnis, M., Moresi, L. 1998. Role of faults, non-linear rheology and viscosity structure in generating plates from instantaneous mantle flow models. J. Geophys. Res. 103, 15255-15268.

Table I: Physical parameters

Symbol	Explanations	Value
A	preexponetial factor (VM-I, II)	2.2866×10^{11} Pa s
	preexponetial factor at 0-410 km (VM-III, IIIa)	2.1484×10^{10} Pa s
	preexponetial factor at 410 km-bottom (VM-III)	2.2866×10^{11} Pa s
	preexponetial factor at 410 km-bottom (VM-IIIa)	2.6093×10^{11} Pa s
	preexponetial factor of granite layer (100L, 102L)	1.7719×10^{8} Pa s
C_p	specific heat	1.2×10^{3} J K^{-1} kg^{-1}
c_F	friction coefficient of fractured material	0.01, 0.02, 0.03
c_Y	friction coefficient of intact material	0.1, 0.2, 0.3
E^*	activation energy (VM-I, II)	240 kJ mol^{-1}
	activation energy at 0-410 km (VM-III, IIIa)	215 kJ mol^{-1}
	activation energy at 410km-bottom (VM-III, IIIa)	240 kJ mol^{-1}
	activation energy of granite layer (100L, 102L)	150 kJ mol^{-1}
g	gravity acceleration	10 m s^{-2}
h	thickness of the model	1320 km
	thickness of the model (Runs 51)	660 km
	thickness of the model (Runs 100L, 102L)	1500 km
k	thermal conductivity	3.96 W m^{-1}
l	horizontal length of the model (20, 50, 100 Ma)	3000, 4000, 6000 km
	horizontal length of the model (100L, 102L)	7500 km
R	gas constant	8.314 J mol^{-1} K^{-1}
T_0	absolute temperature of 0 °C (surface temperature)	273 K
T_h	threshold temperature of the history dependence	345, 177 °C
T_M	mantle potential temperature	1280 °C
V^*	activation volume (VM-I)	0.5×10^{-5} m^3
	activation volume at 0-1320 km (VM-II)	$0.5\text{-}0.25\times10^{-5}$ m^3 mol^{-1}
	activation volume at 0-410 km (VM-III, IIIa)	0.75×10^{-5} m^3 mol^{-1}
	activation volume at 410-1320 km (VM-III)	0.5×10^{-5} m^3 mol^{-1}
	activation volume at 410-1500 km (VM-IIIa)	$0.486\text{-}0.45\times10^{-5}$ m^3 mol^{-1}
Y_0	cohesive strength (Run 51-14, the others)	50, 10 MPa
Y_{max}	maximum yield strength in BDT layer	100-600 MPa

α	thermal expansivity	3.0×10^{-5} K^{-1}
ρ_c	continental crust-mantle density contrast	600 kg m^{-3}
η_{ref}	reference viscosity	5×10^{20} Pa s
η_L	maximum lithosphere viscosity	1×10^{25} Pa s
ρ_0	density	3300 kg m^{-3}

Table II: Runs and Varying Parametes

Run	T, p-dep. viscosity	Friction c_Y	Yield stress Y (MPa)	Friction c_F	Temp. history dep. T_h (ºC, non-dim.)	Initial WZ	Plate-like motion	Other*
Series 50 (yield strength): age of plate=**50** Ma, 4,000×1,320 km, 19 runs								
50-01	VM-I	0.2	200	0.01	T<345 (0.2)	IC1	YES	
50-02	VM-I	0.2	400	0.01	T<345 (0.2)	IC1	YES	
50-03	VM-I	0.2	600	0.01	T<345 (0.2)	IC1	YES	
50-04	VM-I	0.3	200	0.01	T<345 (0.2)	IC1	YES	
50-05	VM-I	0.3	400	0.01	T<345 (0.2)	IC1	YES	
50-06	VM-I	0.3	600	0.01	T<345 (0.2)	IC1	YES	
50-07	VM-I	0.1	200	0.01	T<345 (0.2)	IC1	YES	
50-08	VM-I	0.2	200	0.02	T<345 (0.2)	IC1	NO	
50-09	VM-I	0.2	200	0.03	T<345 (0.2)	IC1	NO	
50-10	VM-I	0.2	200	0.01	T<177 (0.1)	IC1	YES	
50-11	VM-I	0.1	200	0.01	T<345 (0.2)	IC1	NO	1
50-12	VM-I	0.2	200	0.01	T<345 (0.2)	IC1	YES	2
50-13	VM-I	0.2	200	0.01	T<345 (0.2)	IC1	YES	3
50-14	VM-I	0.2	200	0.01	T<345 (0.2)	IC1	YES	4
50-21	VM-I	0.2	100	0.01	T<345 (0.2)	IC2	YES	
50-22	VM-I	0.2	200	0.01	T<345 (0.2)	IC2	NO	
50-23	VM-I	0.3	100	0.01	T<345 (0.2)	IC2	YES	
50-24	VM-I	0.1	200	0.01	T<345 (0.2)	IC2	YES	
50-25	VM-I	0.2	100	0.01	T<345 (0.2)	IC3	NO	

50-26	VM-I	0.1	200	0.01	T<345 (0.2)	IC3	NO	
Series 51 (resolution test): age of plate=**50** Ma, 4,000×660 km, 2 runs								
51-01	VM-I	0.2	200	0.01	T<345 (0.2)	IC1	YES	5
51-02	VM-I	0.2	200	0.01	T<345 (0.2)	IC1	YES	6
Series 52 (viscosity layering): age of plate=**50** Ma, 4,000×1,320 km, 7 runs								
52-01	VM-II	0.1	200	0.01	T<345 (0.2)	IC1	Deformed	
52-02	VM-II	0.2	200	0.01	T<345 (0.2)	IC1	YES	
52-03	VM-III	0.2	200	0.01	T<345 (0.2)	IC1	YES	
52-04	VM-III	0.2	400	0.01	T<345 (0.2)	IC1	YES	
52-05	VM-III	0.2	600	0.01	T<345 (0.2)	IC1	YES	
52-21	VM-II	0.2	200	0.01	T<345 (0.2)	IC2	YES	
52-22	VM-III	0.2	200	0.01	T<345 (0.2)	IC2	YES	
Series 20 (plate age): age of plate=**20** Ma, 3,000×1,320 km, 8 runs								
20-01	VM-I	0.2	200	0.01	T<345 (0.2)	IC1	YES	
20-02	VM-I	0.2	400	0.01	T<345 (0.2)	IC1	YES	
20-03	VM-I	0.2	600	0.01	T<345 (0.2)	IC1	YES	
20-04	VM-I	0.3	200	0.01	T<345 (0.2)	IC1	YES	
20-05	VM-I	0.3	400	0.01	T<345 (0.2)	IC1	YES	
20-06	VM-I	0.3	600	0.01	T<345 (0.2)	IC1	YES	
20-21	VM-I	0.2	200	0.01	T<345 (0.2)	IC2	NO	
20-22	VM-I	0.2	100	0.01	T<345 (0.2)	IC2	YES	
Series 100 (plate age): age of plate=**100** Ma, 6,000×1,320 km, 9 runs								

100-01	VM-I	0.2	200	0.01	T<345 (0.2)	IC1	YES
100-02	VM-I	0.2	400	0.01	T<345 (0.2)	IC1	YES
100-03	VM-I	0.2	600	0.01	T<345 (0.2)	IC1	YES
100-04	VM-I	0.3	200	0.01	T<345 (0.2)	IC1	YES
100-05	VM-I	0.3	400	0.01	T<345 (0.2)	IC1	YES
100-06	VM-I	0.3	600	0.01	T<345 (0.2)	IC1	YES
100-07	VM-I	0.2	200	0.01	T<177 (0.1)	IC1	YES
100-21	VM-I	0.2	200	0.01	T<345 (0.2)	IC2	NO
100-22	VM-I	0.2	100	0.01	T<345 (0.2)	IC2	YES

Series 100L, 102L (long-time intergration): age of plate=**100** Ma, 7,500×1,500 km, 2 runs

100L-01	VM-Ia	0.3	300	0.01	T<345 (0.2)	IC1	YES
102L-01	VM-IIIa	0.3	300	0.01	T<345 (0.2)	IC1	YES
102L-02	VM-IIIa	0.3	300	0.01	T<177 (0.1)	IC1	YES
102L-03	VM-IIIa	0.3	600	0.01	T<345 (0.2)	IC1	YES

*Other features

1: no upwelling plume at the let boundary

2: oceanic overriding plate without the yielding

3: oceanic overriding plate with the yield strength

4: cohesive strength Y_0 = 50 MPa

5: standard resolution: 800×132 control volumes

6: high resolution: 1600×264 control volumes

Figure captions

Fig. 1: A schematic illustration of the model configuration. The top shows the configuration of the initial conditions, and the bottom shows the configuration after slab development. The dark areas in the uppermost area show subducting and overriding plates. (a) The initial conditions include a preexisiting weak zone in the most of the models. (b) After slab development, a segment with small yield strength (the hatched area) is formed on the surface of the subducting plate by the hysteresis-dependent rheology. The fractured segment acts as a fault zone at the plate boundary as the subducted slab grows. The star shows the location of first yielding.

Fig. 2: The viscosity-depth profile for the short time-integration models. VM-I: a standard model with a constant activation volume, VM-II: a weakly depth-dependent viscosity model whose activation volume decreases linearly with depth, VM-III: a model with a low-viscosity asthenosphere.

Fig. 3: The rheology model of fresh (unfractured) segments of the lithosphere. There are three rheological layers: a brittle layer, a brittle-ductile transition layer and a viscous layer. The strain rate for calculating viscous strength is assumed to be 10^{-15} s^{-1}.

Fig. 4: The hysteresis curve of the "fault zone segment." The solid line shows the yield strength of fresh materials. The materials in this layer remember past fractures and their strength is reduced to the level shown by the dotted line. We assume that strength recovers at the depth of 330 km.

Fig. 5: A schematic illustration of the configuration of the initial weak zone. The hatched area between the solid lines consists of a fractured fault-zone segment with a weak yield strength. The dark area between the dashed

lines consists of a fresh fault-zone segment with the same initial strength as the ambient mantle but with hysteresis-dependent rheology. (a) IC1, a fractured fault-zone segment across the whole lithosphere. (b) IC2, a fractured fault-zone segment with weak strength reaching the bottom of the continental crust (35 km). (c) IC3, a fresh fault-zone segment across the whole lithosphere.

Fig. 6: Evolution of Run 50-01 (A_P = 50 Ma, VM-I, c_y = 0.2 Y_{max} = 200 MPa). The surface velocity (cm yr^{-1}) is shown by the graph. The positive value indicates velocity to the right. The viscosity (Pa·s) is shown by the contour lines in the logarithmic scale. The contour intervals are set at 1.

Fig. 7: A snapshot of Run 50-01 (A_P = 50 Ma, VM-I, c_y = 0.2, Y_{max} = 200 MPa) in 46 Myr. From the top, the surface velocity (cm yr^{-1}), the temperature (250 °C intervals), the viscosity in the logarithmic scale (1 intervals), and streamlines (5×10^{-5} m^2 s^{-1} intervals) are shown.

Fig. 8: Summary of effects of the internal plate strength and the initial weak zone. The symbols show the conditions in which subduction begins. Circles (IC1): subduction initiates only from IC1 (see Fig. 4). Squares (IC2): subduction initiates from IC2. Diamonds (IC2+): No subduction in a VM-I model, and subduction in VM-II and VM-III models with IC2. The vertical axis shows the friction coefficient of the plate (c_Y) and the horizontal axis shows the maximum yield strength of the plate (Y_{max}).

Fig. 9: Evolution of the velocity of the subducting plate with various initial ages and strengths. The colours show the plate age in the initial condition: red: 20 Ma, blue: 50 Ma, green: 100 Ma. The solid and dashed lines show the internal strength of the plate: solid line c_y = 0.2, Y_{max} = 200 MPa: dashed line: c_y = 0.3, Y_{max} = 600 MPa. The horizontal axis shows the elapsed

time (Myr) and the vertical axis shows the velocity (cm yr^{-1}).

Fig. 10: Stress fields of Run 50-01 (A_P = 50 Ma, c_y = 0.2, Y = 200 MPa) in 41 Myr. Top: maximum differential stress (σ_1-σ_3), bottom: horizontal normal stress (σ_{xx}). The colour scales show the stress. The positive values are in blue and the negative values are in red. The thick green line indicates the bottom of the lithospere defined by $T < 950$ °C or $\eta > 3 \times 10^{22}$.

Fig. 11: (a) Evolution of the slab depth and velocity of the subducting plate. (b) Evolution of driving and resisting forces working in or onto the plate for Run 50-01 (A_P = 50 Ma, VM-I, c_y = 0.2, Y_{max} = 200 MPa). The horizontal axes show the elapsed time (Myr). The vertical axes show (a): depth of the slab tip (km) and velocity of the subduction plate (cm yr^{-1}), and (b): amplitude of the force per unit length perpendicular to the plate motion (N m^{-1}).

Fig. 12: A snapshot of Run 52-01 (A_P = 50 Ma, VM-I, c_y = 0.1, Y = 200 MPa) in 9 Myr and Run 52-03 (A_P = 50 Ma, VM-III, c_y = 0.2, Y_{max} = 200 MPa) in 13 Myr. The meaning and the scales are the same as those of Fig. 7.

Fig. 13: Horizontal flow velocity profile of Run 50-01 (VM-I) and Run 52-03 (VM-III) at the centre of the subducting plate (x = 1500 km). The velocity is normalized by that of the subducting plate, which is shown in the legend. The solid lines with closed and open squares show the velocities of Run 50-01 in 30 Myr and 46 Myr, respectively. The dashed lines with open and closed triangles show velocities of Run 52-03 in 5 Myr and 20 Myr, respectively.

Fig. 14: Evolution of driving and resisting mantle-drag forces. The meaning of the axes is the same as in Fig. 13b. In Run 52-03 (VM-III, lines with squares), the bottom of the plate is defined by the 950 K isotherm because viscosity has a weaker temperature dependence than in Run 50-01 (VM-I, lines with circles).

Fig. 15: Evolution of the viscosity field for Run 100L-03, a long-time integration model. The colour scale shows the viscosity. The lower layer with imposed temperature (see section 3.5) is not shown in the snapshots.

Fig. 16: Evolution of the subducting plate velocity for Runs 100L-01 (VM-Ia, Y = 300 MPa, T_h < 345 °C; the solid line with closed squares), 102L-01 (VM-IIIa, Y_{max} = 300 MPa, T_h < 345 °C; the dashed line with open squares), 102L-02 (VM-IIIa, Y_{max} = 300 MPa, T_h < 177 °C; the dashed line with open squares), and 102L-03 (VM-IIIa, Y_{max} = 600 MPa, T_h < 345 °C; the dashed line with open squares). The horizontal axis shows the elapsed time (Myr) and the vertical axis shows the velocity (cm yr^{-1}). The velocity fluctuation is generated by deformation of the subducted slab caused by viscosity layering.

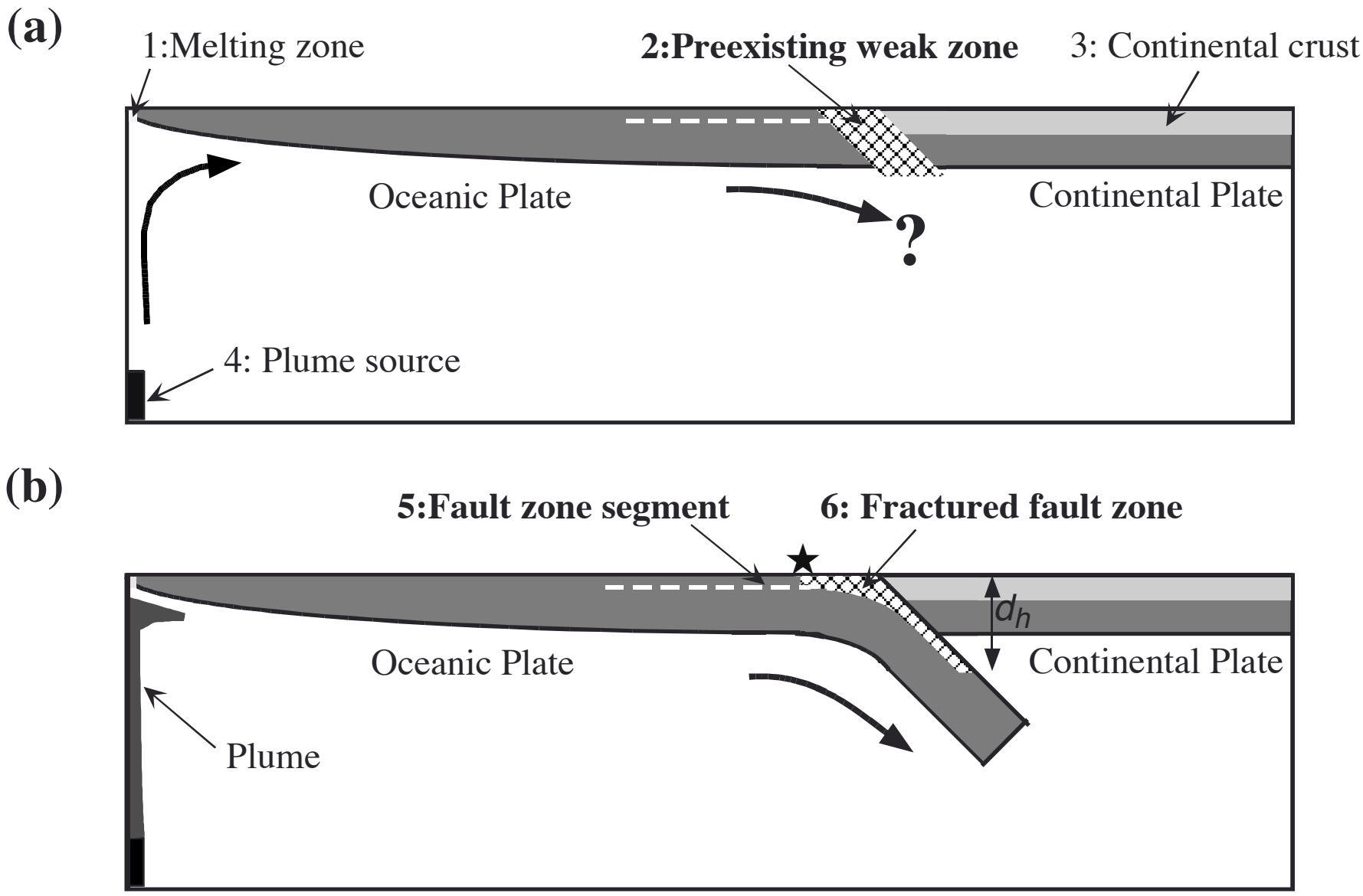
(a)
1:Melting zone
2:Preexisting weak zone
3: Continental crust
Oceanic Plate
Continental Plate
?
4: Plume source
(b)
5:Fault zone segment
6: Fractured fault zone
d_h
Oceanic Plate
Continental Plate
Plume

Fig. 1

Fig. 2

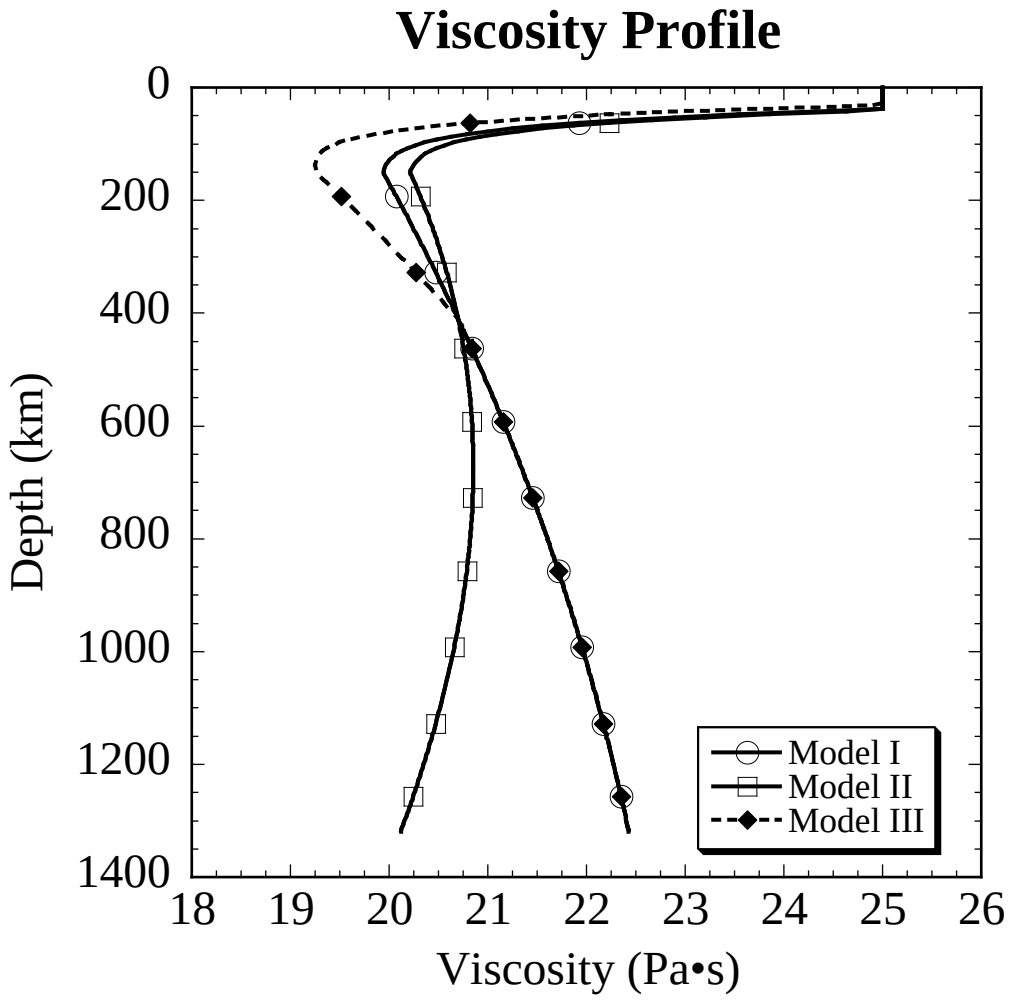
Viscosity Profile
Depth (km)
0
200
400
600
800
1000
1200
1400
18
19
20
21
22
23
24
25
26
Viscosity (Pa•s)
Model I
Model II
Model III

Fig. 3

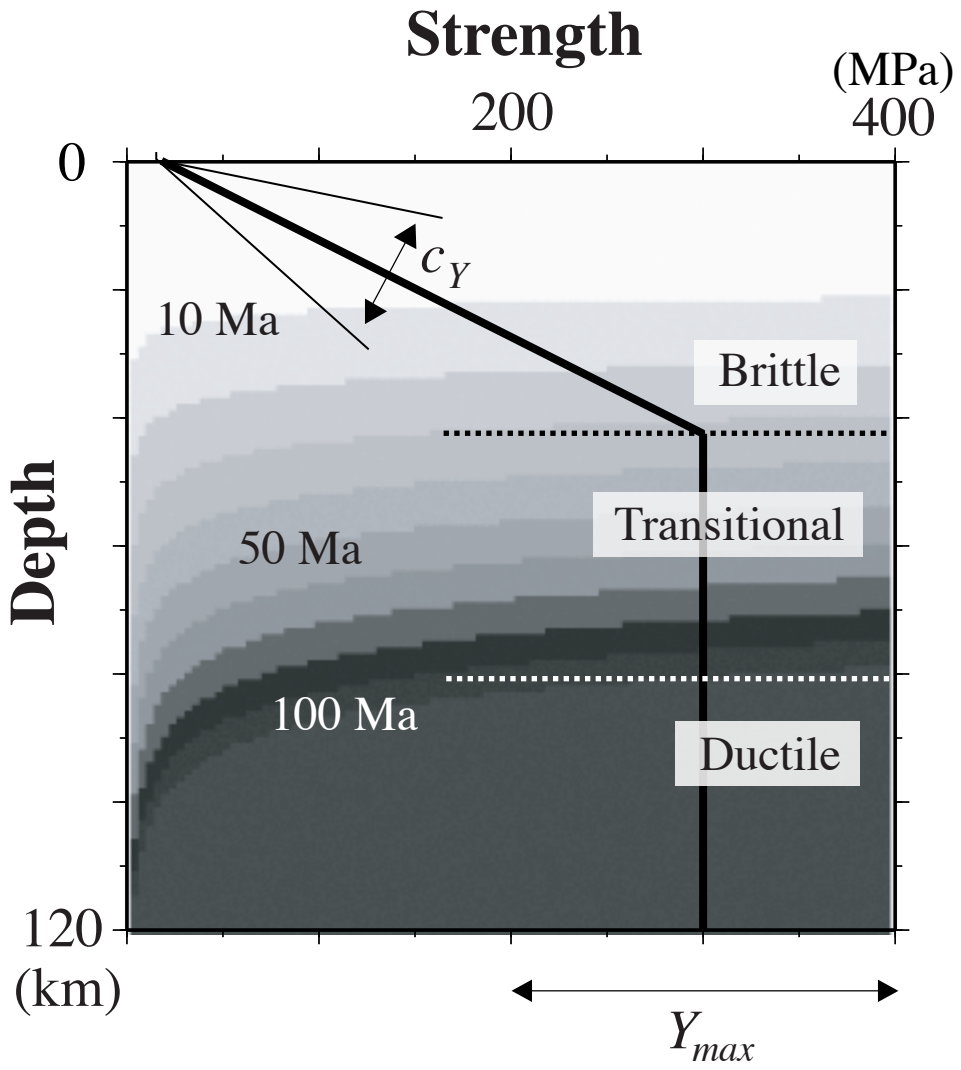
Strength
(MPa)
200
400
0
120
(km)
Depth
c_Y
10 Ma
50 Ma
100 Ma
Brittle
Transitional
Ductile
Y_{max}

Fig. 4

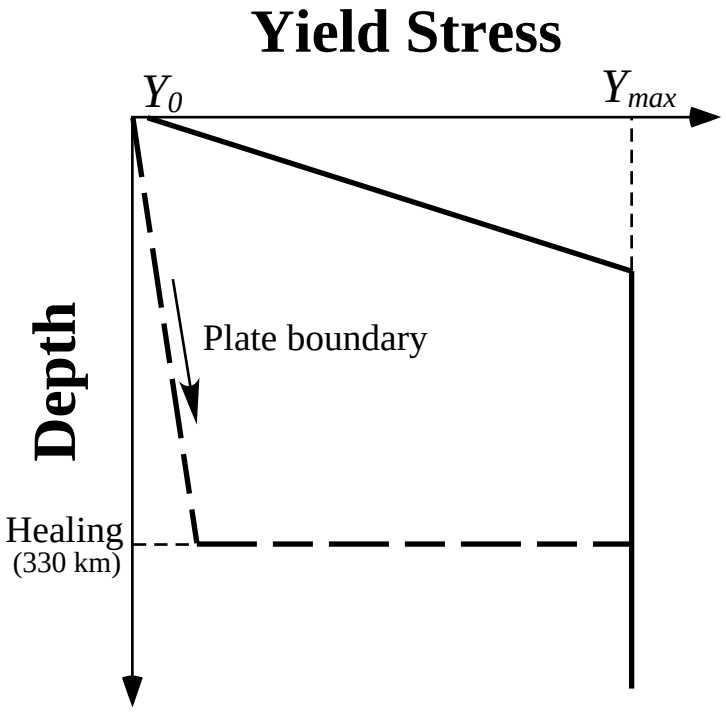

Fig. 5

(a) IC1

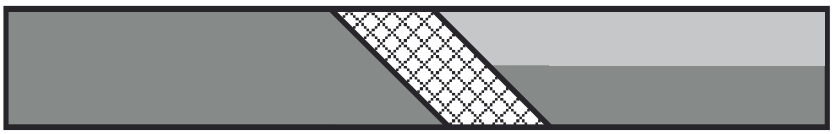

(b) IC2

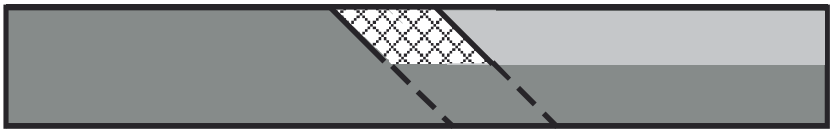

(c) IC3

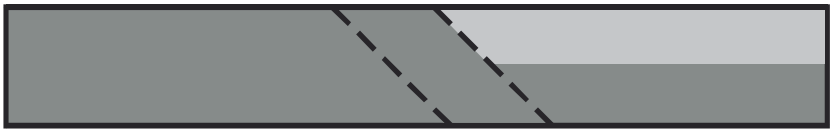

Fig. 6

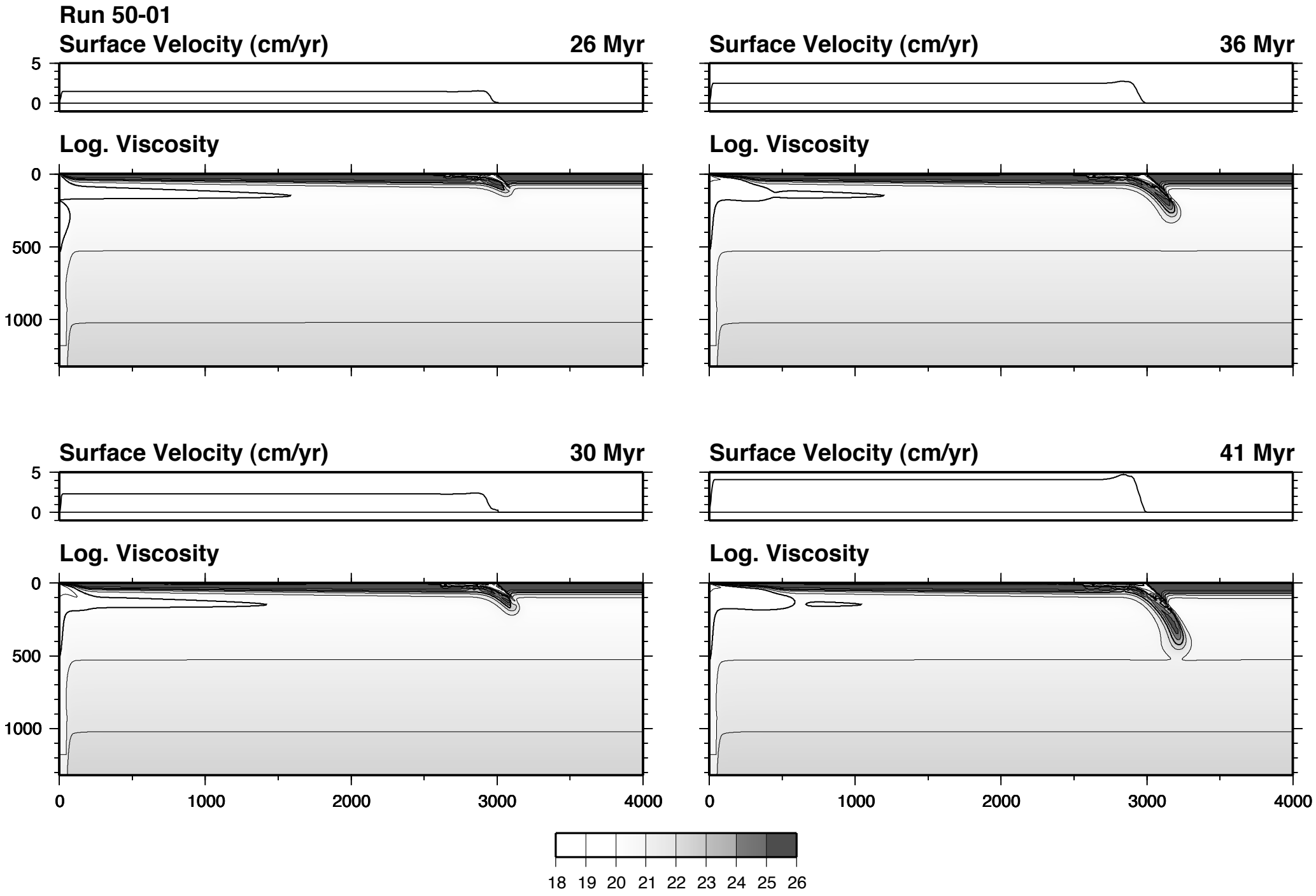
Run 50-01
Surface Velocity (cm/yr)
26 Myr
5
0
Log. Viscosity
0
500
1000
Surface Velocity (cm/yr)
36 Myr
Log. Viscosity
Surface Velocity (cm/yr)
30 Myr
5
0
Log. Viscosity
0
500
1000
Surface Velocity (cm/yr)
41 Myr
Log. Viscosity
0
1000
2000
3000
4000
0
1000
2000
3000
4000
18 19 20 21 22 23 24 25 26

Fig. 7

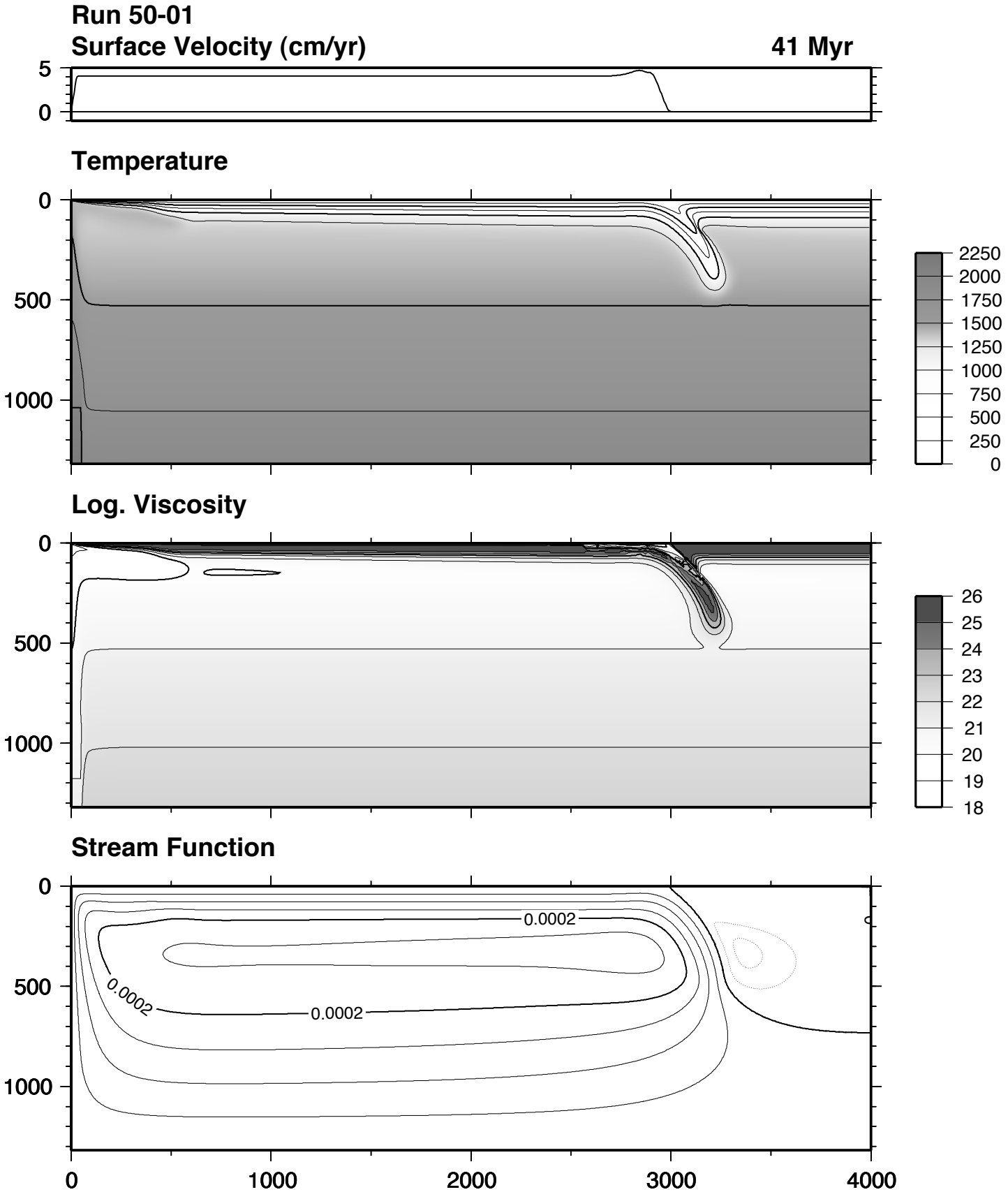
Run 50-01
Surface Velocity (cm/yr)
41 Myr
5
0
Temperature
0
500
1000
2250
2000
1750
1500
1250
1000
750
500
250
0
Log. Viscosity
0
500
1000
26
25
24
23
22
21
20
19
18
Stream Function
0
500
1000
0.0002
0.0002
0.0002
0
1000
2000
3000
4000

Fig. 8

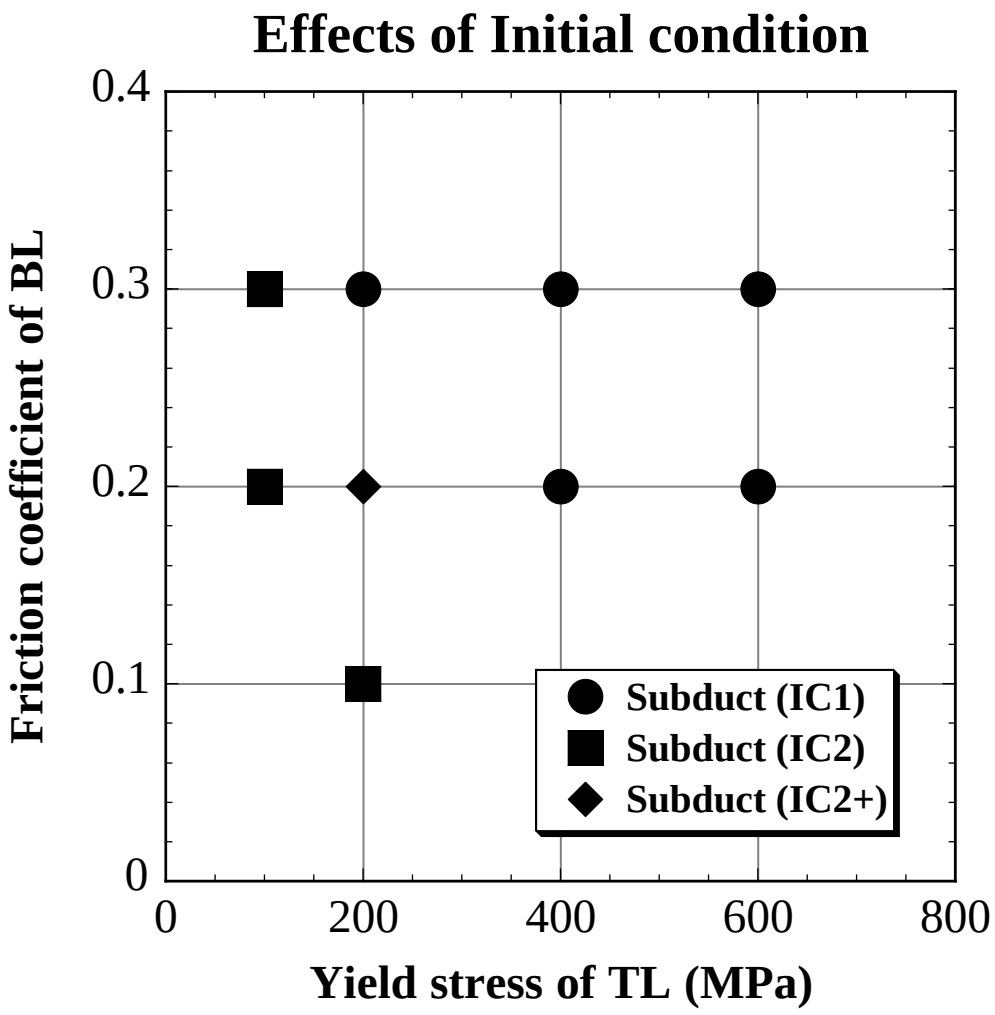
Effects of Initial condition
Friction coefficient of BL
0.4
0.3
0.2
0.1
0
0
200
400
600
800
Yield stress of TL (MPa)
Subduct (IC1)
Subduct (IC2)
Subduct (IC2+)

Fig. 9

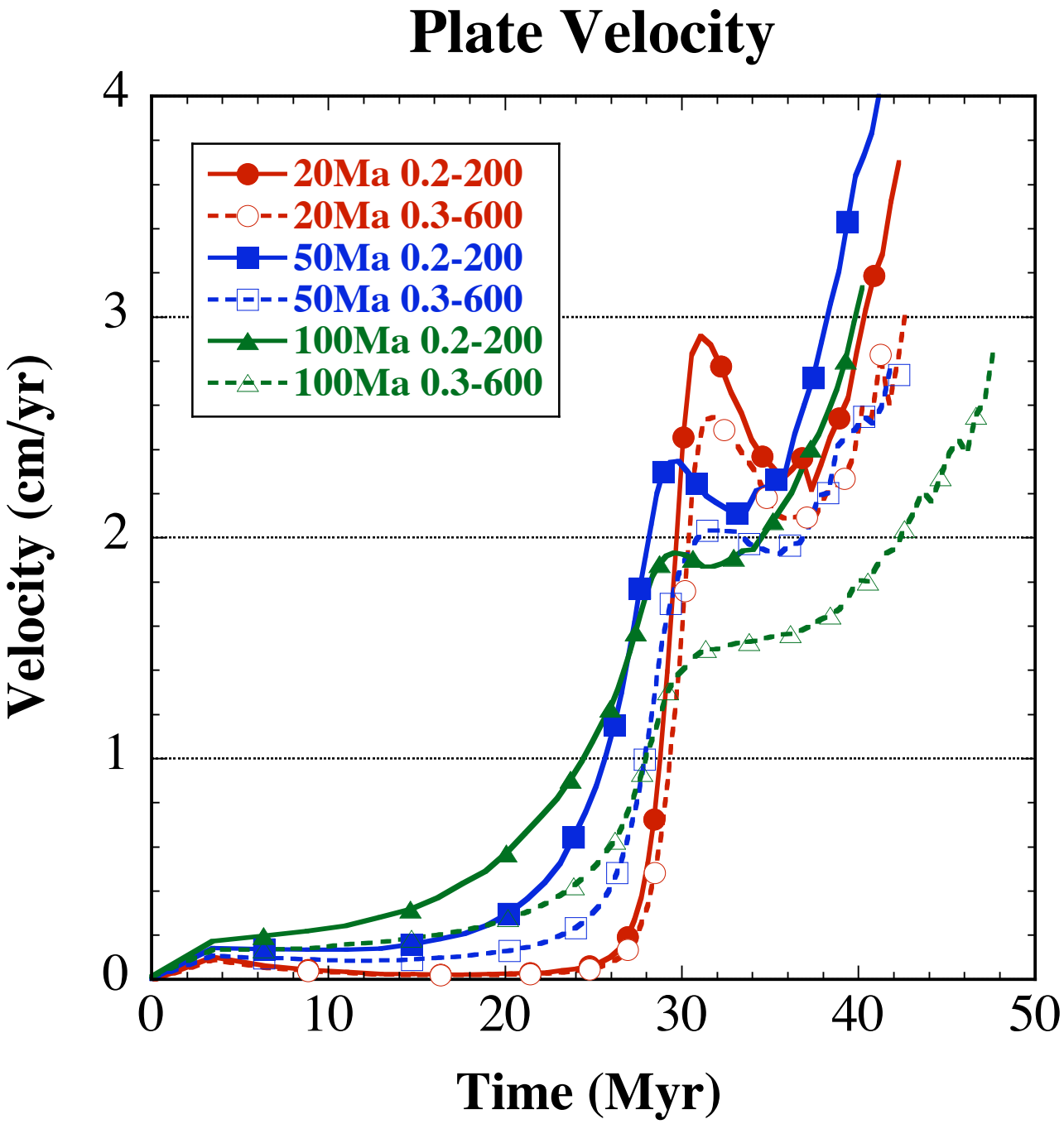
Plate Velocity
20Ma 0.2-200
20Ma 0.3-600
50Ma 0.2-200
50Ma 0.3-600
100Ma 0.2-200
100Ma 0.3-600
Velocity (cm/yr)
Time (Myr)
0
1
2
3
4
0
10
20
30
40
50

Fig. 10

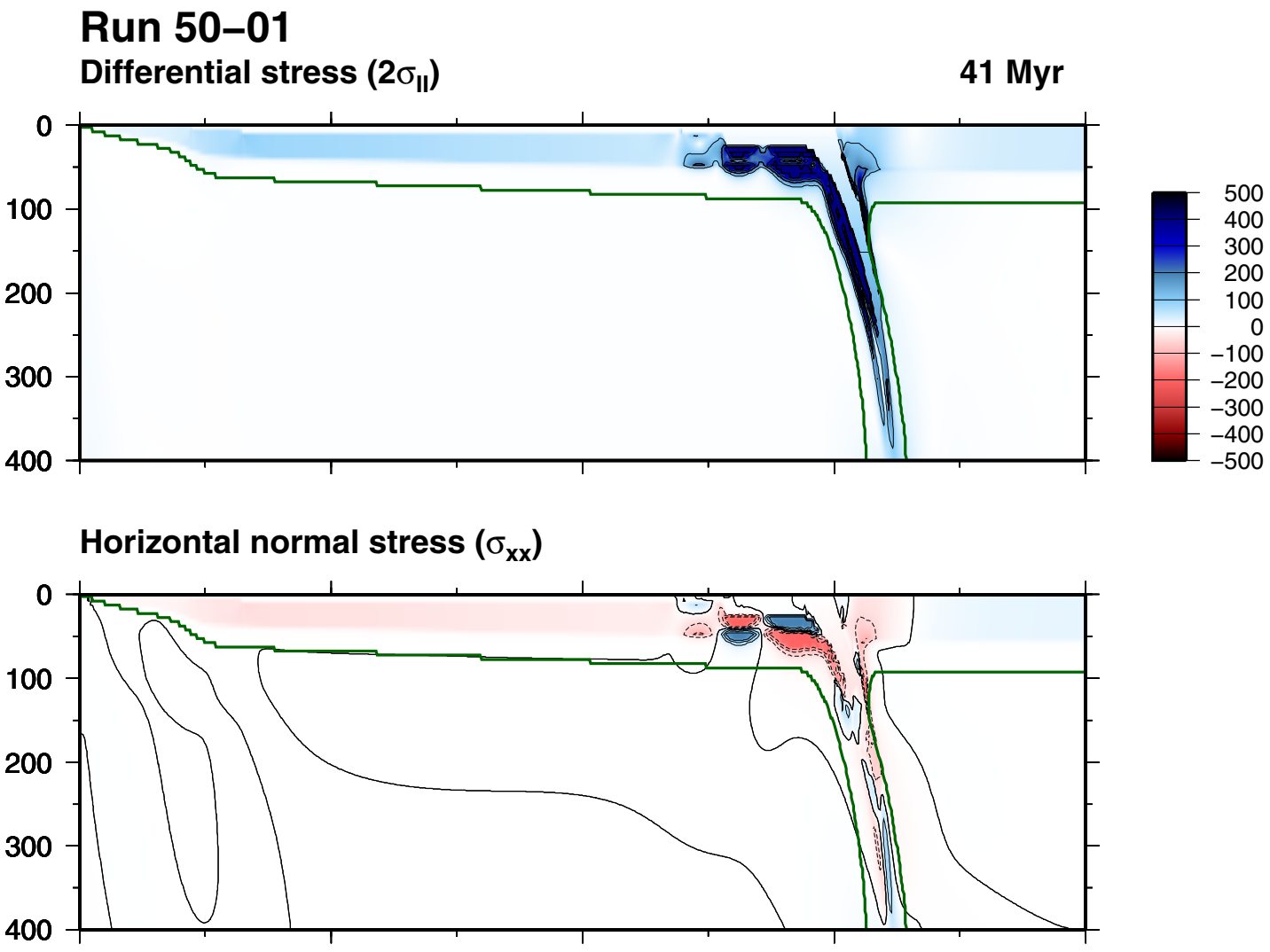
Run 50–01
Differential stress ($2\sigma_{II}$)
41 Myr
0
100
200
300
400
500
400
300
200
100
0
−100
−200
−300
−400
−500
Horizontal normal stress (σ_{xx})
0
100
200
300
400

Fig 11 (a)

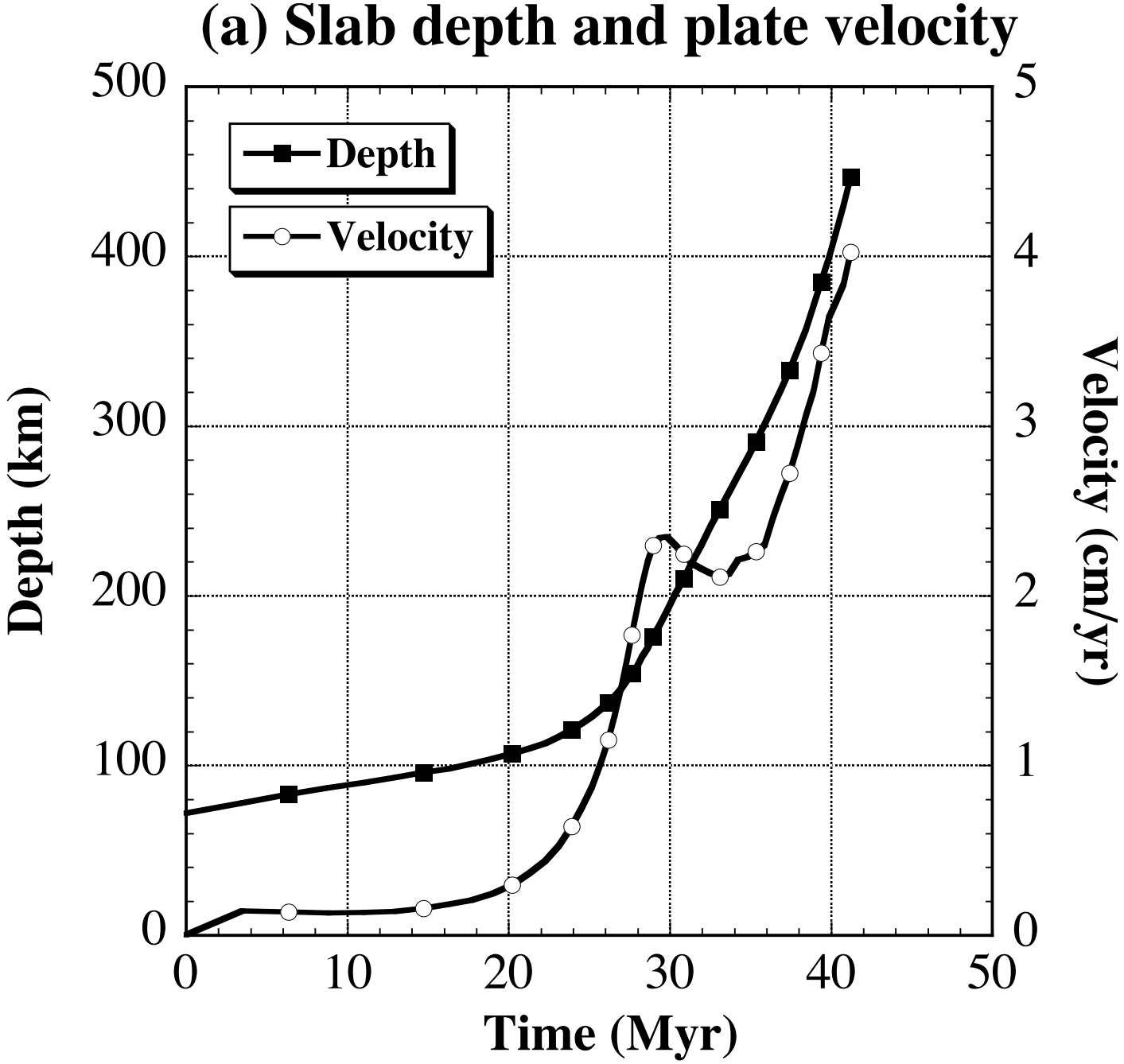
(a) Slab depth and plate velocity
Depth
Velocity
Depth (km)
Velocity (cm/yr)
Time (Myr)
0
100
200
300
400
500
0
1
2
3
4
5
0
10
20
30
40
50

Fig. 11 (b)

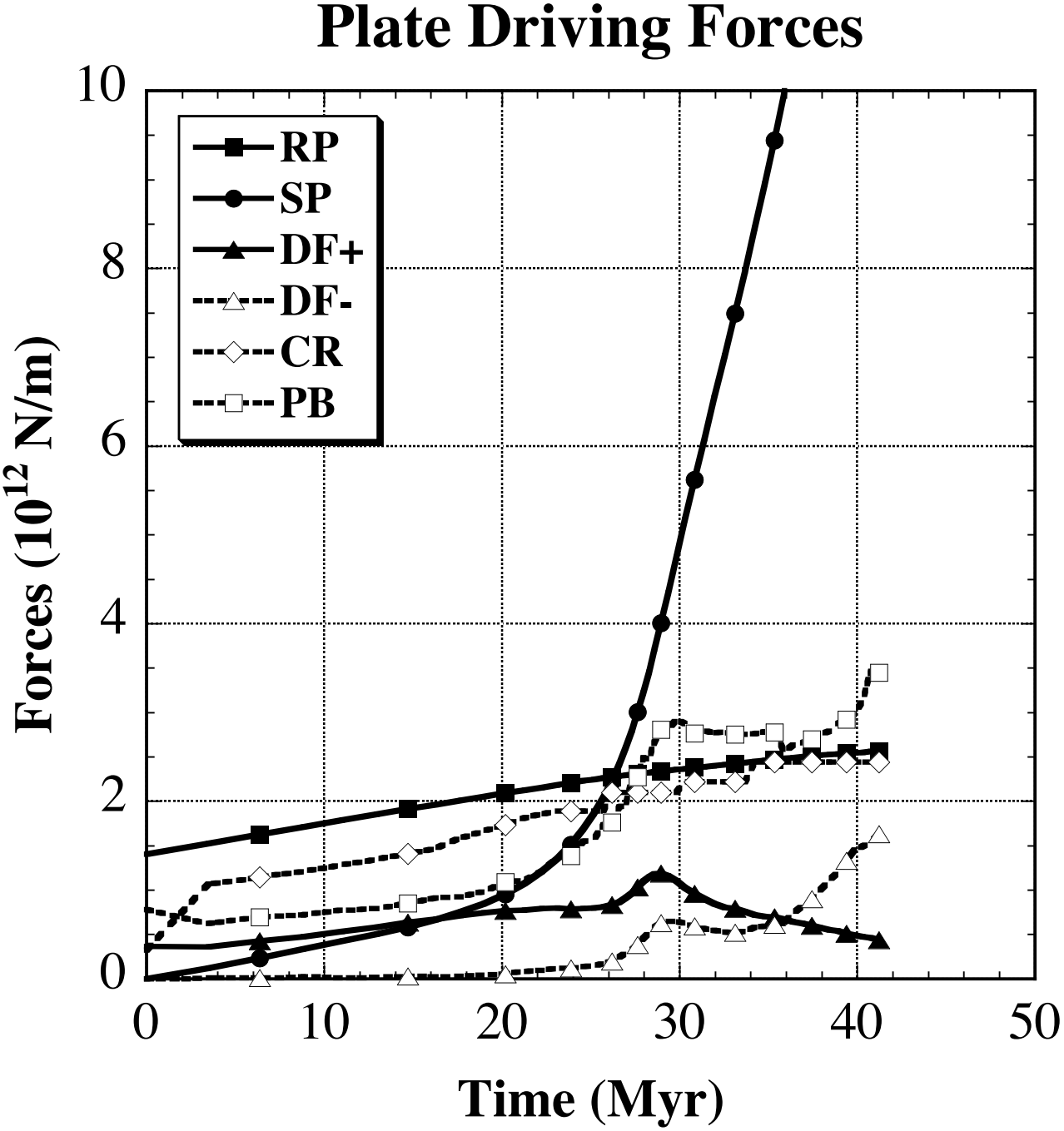
Plate Driving Forces
RP
SP
DF+
DF-
CR
PB
Forces (10^{12} N/m)
Time (Myr)
0
2
4
6
8
10
0
10
20
30
40
50

Fig. 12

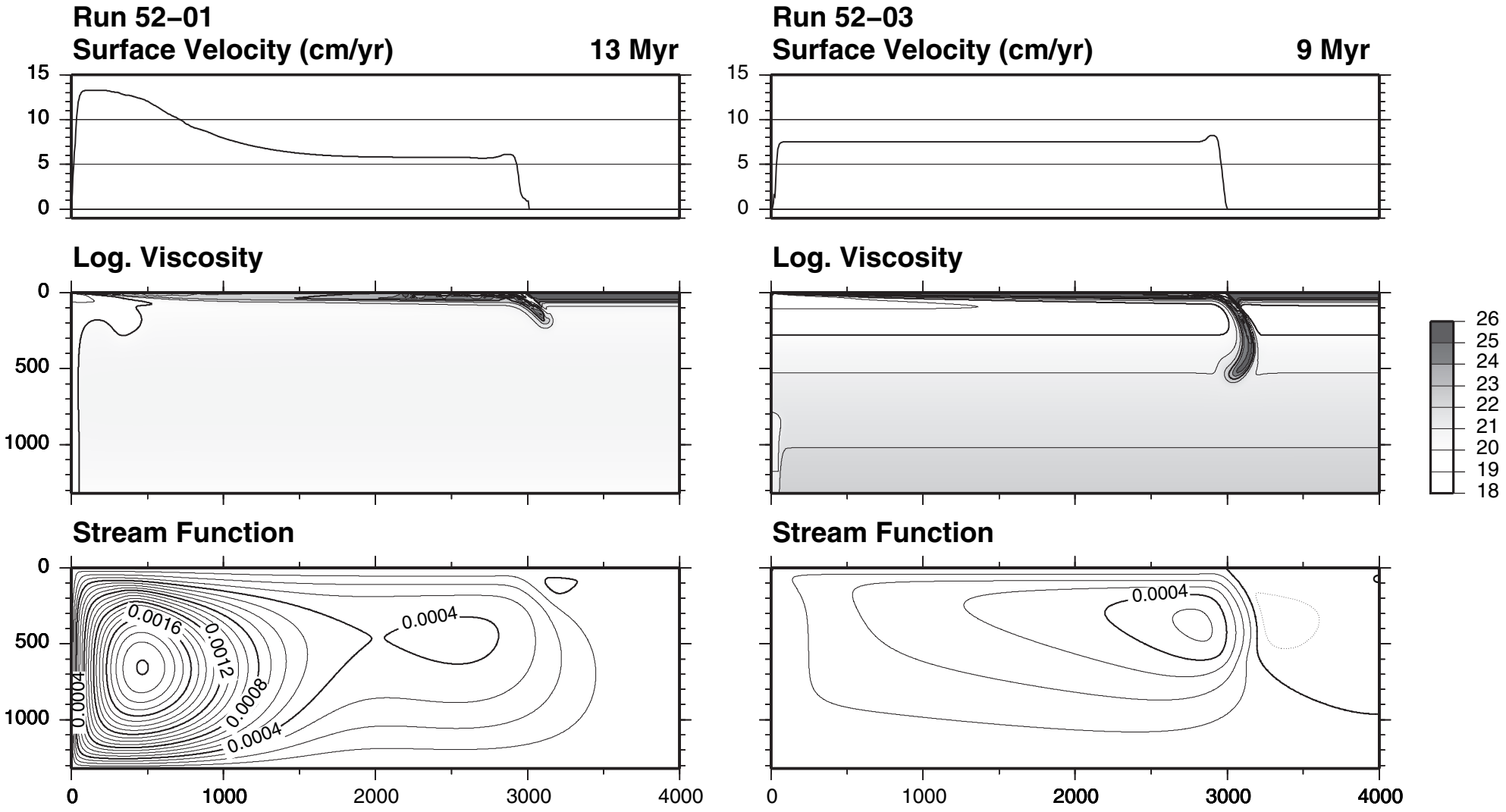
Run 52–01
Surface Velocity (cm/yr)
13 Myr
15
10
5
0
Log. Viscosity
0
500
1000
Stream Function
0.0016
0.0012
0.0008
0.0004
0.0004
0.0004
0
1000
2000
3000
4000
Run 52–03
Surface Velocity (cm/yr)
9 Myr
15
10
5
0
Log. Viscosity
Stream Function
0.0004
0
1000
2000
3000
4000
26
25
24
23
22
21
20
19
18

Fig. 13

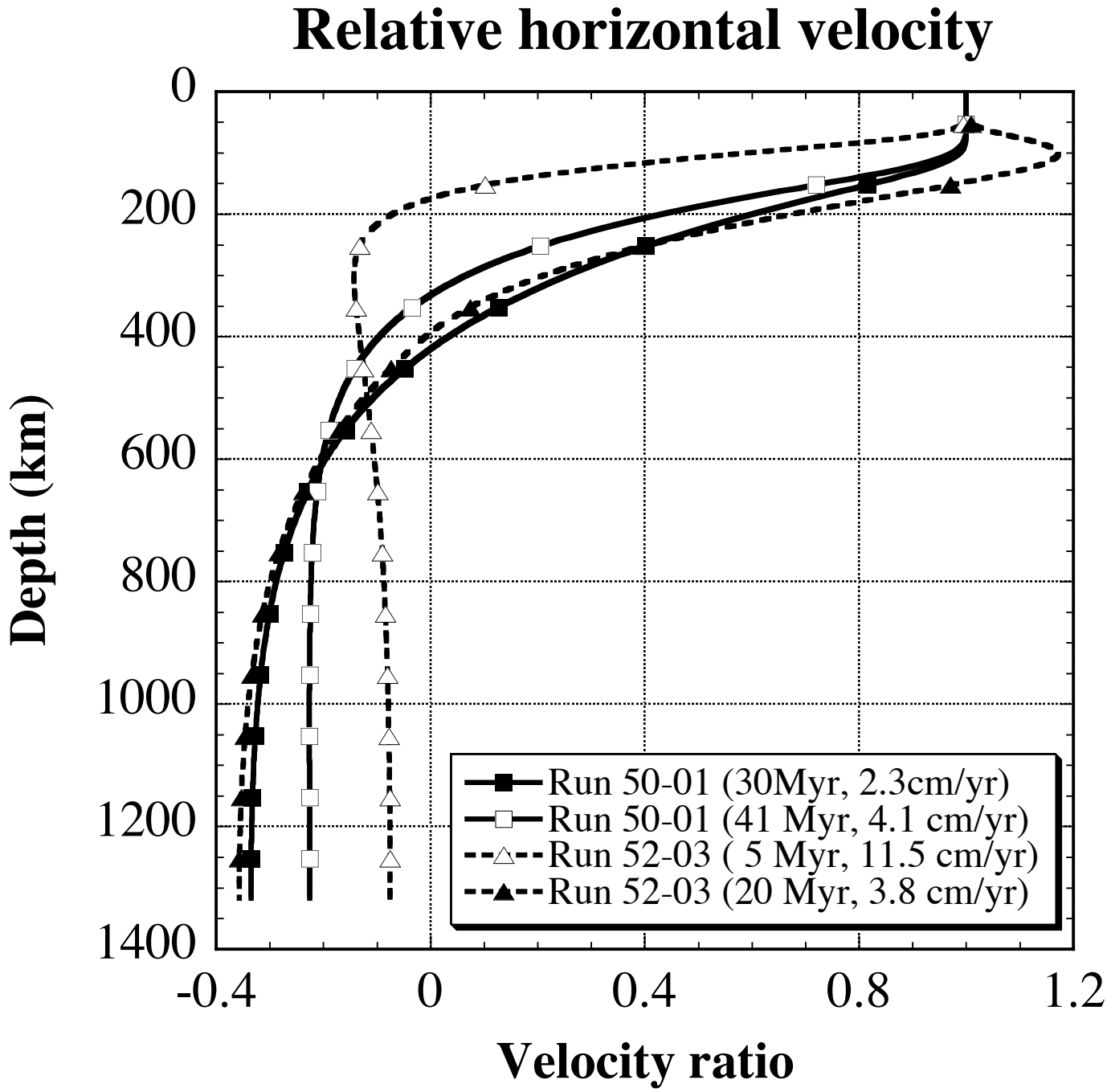
Relative horizontal velocity
Depth (km)
0
200
400
600
800
1000
1200
1400
-0.4
0
0.4
0.8
1.2
Velocity ratio
Run 50-01 (30Myr, 2.3cm/yr)
Run 50-01 (41 Myr, 4.1 cm/yr)
Run 52-03 (5 Myr, 11.5 cm/yr)
Run 52-03 (20 Myr, 3.8 cm/yr)

Fig. 14

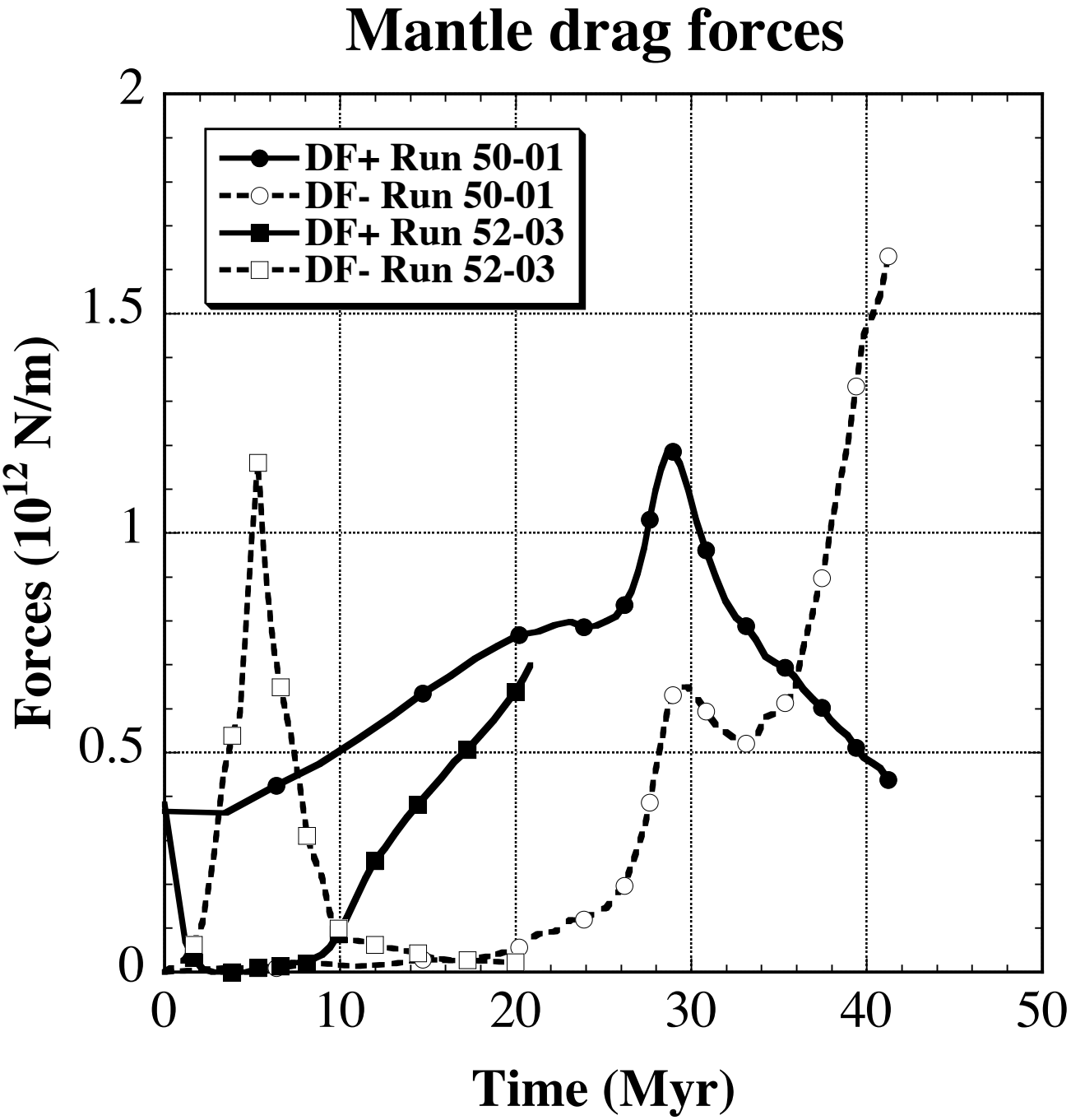
Mantle drag forces
DF+ Run 50-01
DF- Run 50-01
DF+ Run 52-03
DF- Run 52-03
Forces (10^{12} N/m)
Time (Myr)
0
0.5
1
1.5
2
0
10
20
30
40
50

Fig. 15

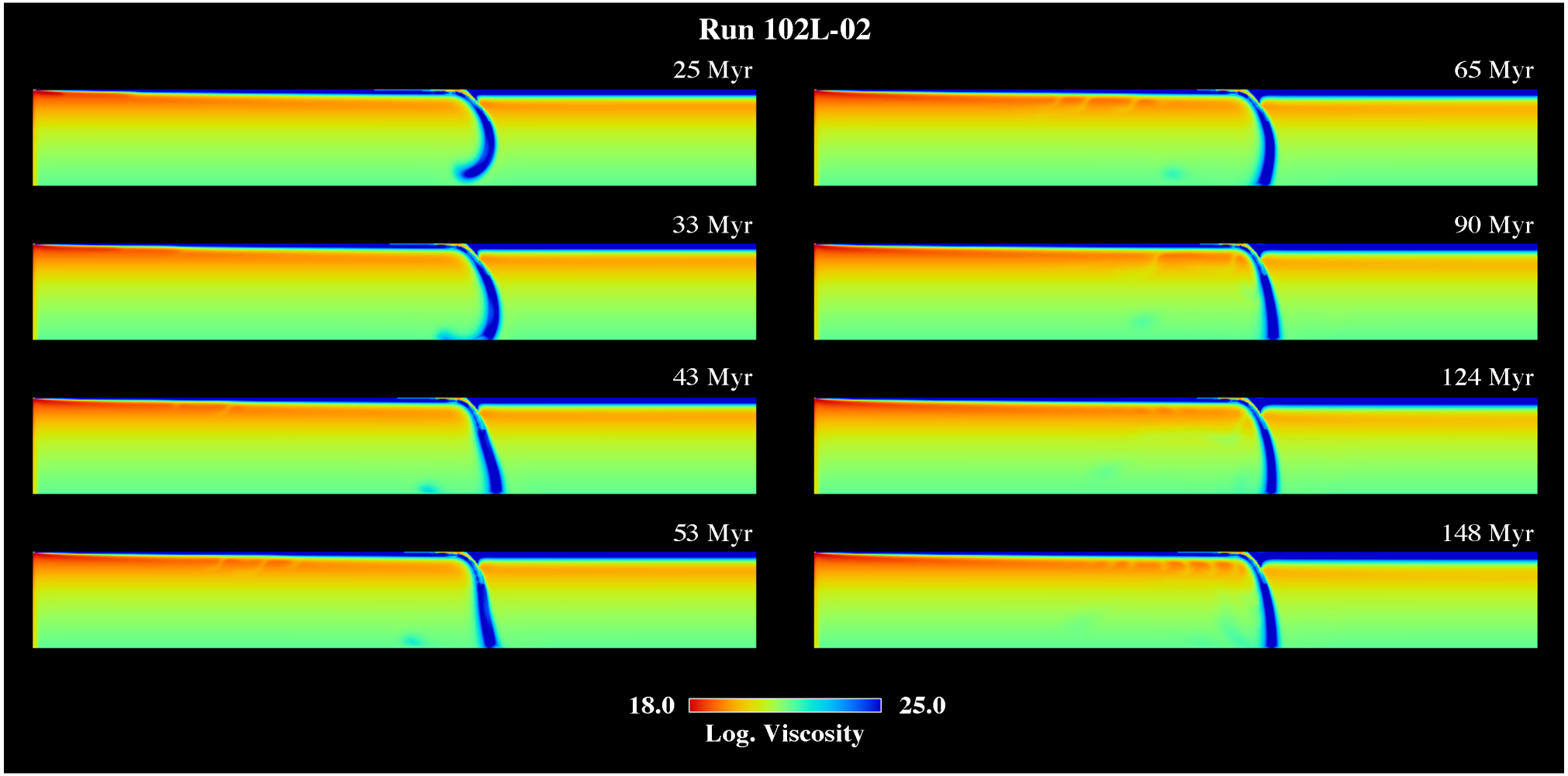
Run 102L-02
25 Myr
65 Myr
33 Myr
90 Myr
43 Myr
124 Myr
53 Myr
148 Myr
18.0
25.0
Log. Viscosity

Fig. 16

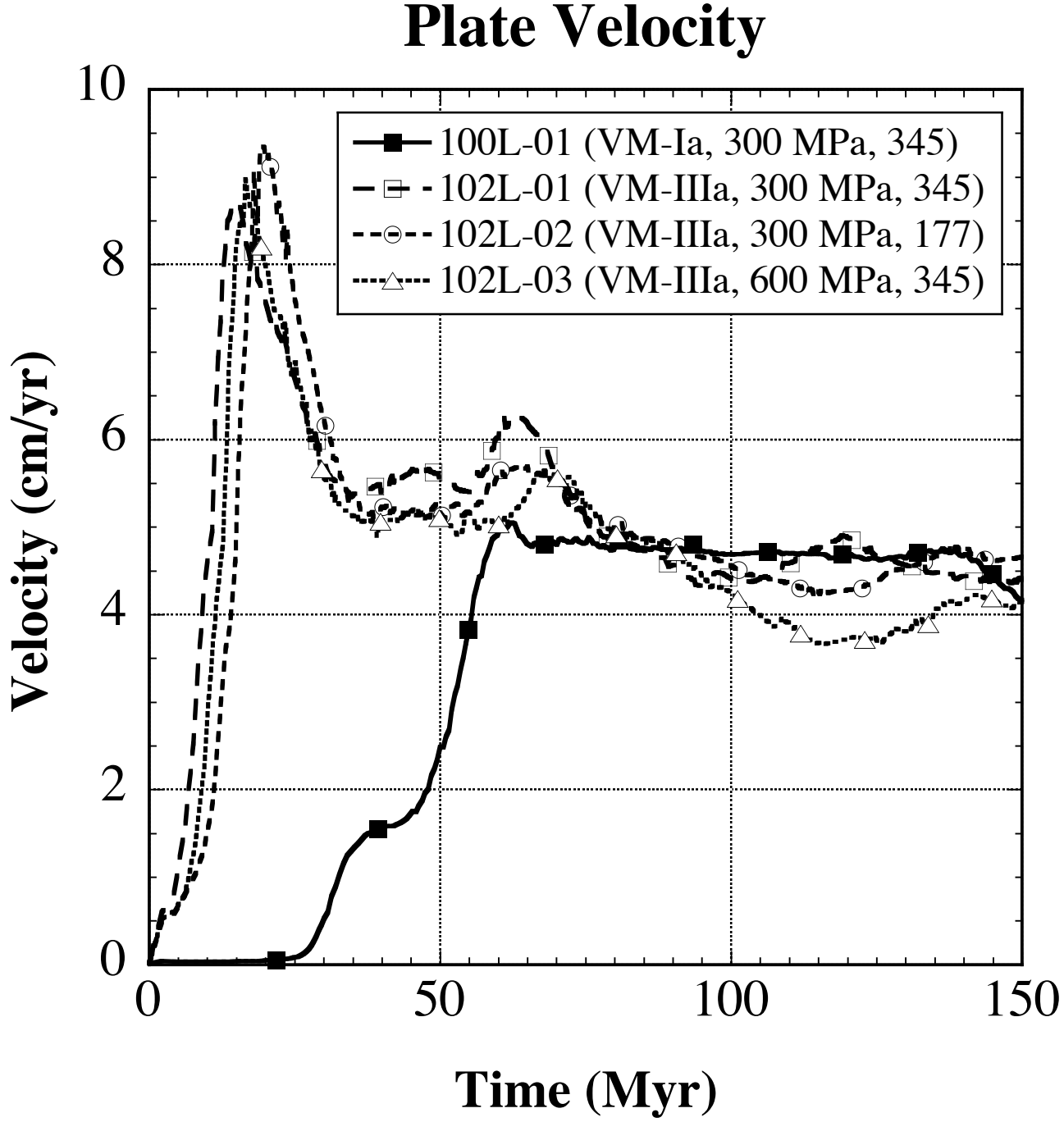
Plate Velocity
100L-01 (VM-Ia, 300 MPa, 345)
102L-01 (VM-IIIa, 300 MPa, 345)
102L-02 (VM-IIIa, 300 MPa, 177)
102L-03 (VM-IIIa, 600 MPa, 345)
Velocity (cm/yr)
Time (Myr)
0
2
4
6
8
10
0
50
100
150